THE GEOLOGICAL SOCIETY OF AMERICA®

Examining the influence of disequilibrium landscape on millennial-scale erosion rates in the San Bernardino Mountains, California, USA

Marina O. Argueta[1], Seulgi Moon[1,†], Kimberly Blisniuk[2], Nathan D. Brown[3], Lee B. Corbett[4], Paul R. Bierman[4], and Susan R.H. Zimmerman[5]

[1]*Department of Earth, Planetary, and Space Sciences, University of California, Los Angeles, 595 Charles E. Young Drive East, Los Angeles, California 90095, USA*

[2]*Department of Geology, San Jose State University, One Washington Square, San Jose, California 95192, USA*

[3]*Department of Earth and Environmental Sciences, University of Texas, 107 Geoscience Building, Arlington, Texas 76019, USA*

[4]*Rubenstein School of Environment and Natural Resources, University of Vermont, 86 Brookes Avenue, Burlington, Vermont 05405, USA*

[5]*Center for Accelerator Mass Spectrometry, Lawrence Livermore National Laboratory, 7000 East Avenue, L-397, Livermore, California 94550, USA*

ABSTRACT

Temporal and spatial variations of tectonic rock uplift are generally thought to be the main controls on long-term erosion rates in various landscapes. However, rivers continuously lengthen and capture drainages in strike-slip fault systems due to ongoing motion across the fault, which can induce changes in landscape forms, drainage networks, and local erosion rates. Located along the restraining bend of the San Andreas Fault, the San Bernardino Mountains provide a suitable location for assessing the influence of topographic disequilibrium from perturbations by tectonic forcing and channel reorganization on measured erosion rates. In this study, we measured 17 new basin-averaged erosion rates using cosmogenic ^{10}Be in river sands (hereafter, ^{10}Be-derived erosion rates) and compiled 31 ^{10}Be-derived erosion rates from previous work. We quantify the degree of topographic disequilibrium using topographic analysis by examining hillslope and channel decoupling, the areal extent of pre-uplift surface, and drainage divide asymmetry across various landscapes. Similar to previous work, we find that erosion rates generally increase from north to south across the San Bernardino Mountains, reflecting a southward increase in tectonic activity. However, a comparison between ^{10}Be-derived erosion rates and various topographic metrics in the southern San Bernardino Mountains suggests that the presence of transient landscape features such as relict topography and drainage-divide migration may explain local variations in ^{10}Be-derived erosion rates. Our work shows that coupled analysis of erosion rates and topographic metrics provides tools for assessing the influence of tectonic uplift and channel reorganization on landscape evolution and ^{10}Be-derived erosion rates in an evolving strike-slip restraining bend.

INTRODUCTION

The spatial distribution and temporal evolution of erosion rates across landscapes in strike-slip restraining bends provide insight into fault activity and potential seismic hazards (Cunningham and Mann, 2007; Gudmundsdottir et al., 2013; Cochran et al., 2017; Collett et al., 2019). Previous studies from different mountain ranges adjacent to the restraining bends of the San Andreas Fault, California, USA, show that million-year and millennial-scale erosion rates from low-temperature thermochronometry and cosmogenic radionuclides, respectively, increase with topographic metrics such as hillslope gradients, channel steepness, and fluvial relief (Spotila et al., 2002; Binnie et al., 2008, 2010; Gudmundsdottir et al., 2013; Moon et al., 2018; Baden et al., 2022). Based on an assumption of steady-state landscapes, prior work used basin-averaged erosion rates over millennial time scales estimated from cosmogenic nuclides (hereafter, ^{10}Be-derived erosion rates) to infer the spatial patterns and magnitude of tectonic uplift driven by transpression along restraining bends (e.g., Gudmundsdottir et al., 2013).

However, spatial and temporal changes of tectonic rock uplift and drainage networks along strike-slip restraining bends may induce topographic disequilibrium and complicate the interpretation of ^{10}Be-derived erosion rates (Binnie et al., 2007, 2008, 2010; Norton et al., 2008; Willenbring et al., 2013; Moon et al., 2018). The stress field within restraining bends may evolve over time and can induce temporal changes in slip rates and locations of active fault segments and strands (Weldon and Sieh, 1985; Niemi and Hall, 1992; Matti and Morton, 1993; Behr et al., 2010; Blisniuk et al., 2010, 2013; Cooke and Dair, 2011; McGill et al., 2013, 2021). For example, the Mendocino Triple Junction region and the San Bernardino Mountains preserve evidence of transient topographic disequilibrium features, such as pre-uplift, relict topography, which indicates that the landscape is still adjusting to temporal changes in tectonic uplift rates (Binnie et al., 2007, 2008, 2010; Willenbring et al., 2013; Moon et al., 2018; Fig. 1).

In addition, rivers along and across strike-slip faults are subject to ongoing changes in base level due to tectonic forcing (e.g., fault displacement) or dynamic river processes (e.g., lengthening and capture) (Duvall and Tucker, 2015; Duvall et al., 2020; Dascher-Cousineau et al., 2021). These perturbations can lead to changes in longitudinal channel profiles, plan-view channel geometries, and topologies, which can drive drainage network reorganization and headward divide migration (Willett et al., 2014; Duvall and Tucker, 2015; Duvall et al., 2020). In areas with transient topographic disequilibrium, the assumptions for estimating ^{10}Be-derived erosion rates from detrital river sands (e.g., complete mixing of sediments within a basin

Seulgi Moon https://orcid.org/0000-0001-5207-1781

†sgmoon@ucla.edu

GSA Bulletin;
published online 17 August 2023

https://doi.org/10.1130/B36734.1; 9 figures; 1 supplemental file.

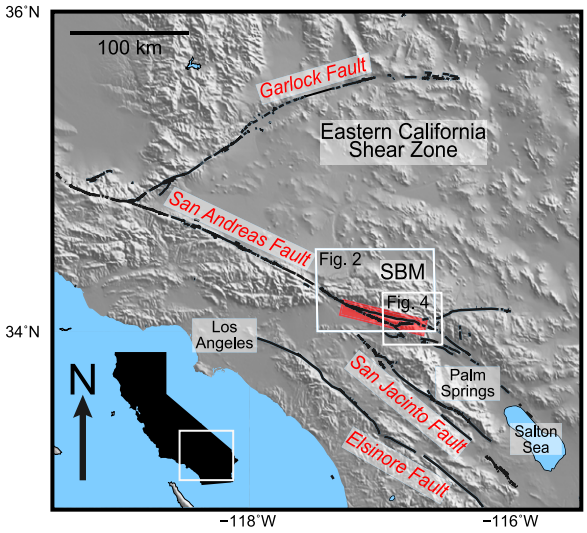

Figure 1. Hillshade map of southern California with major faults, including the San Andreas, Garlock, San Jacinto, and Elsinore faults, shown by black lines. The restraining bend of the southern San Andreas Fault, which runs through the San Bernardino Mountains (SBM), is highlighted in red. White rectangles indicate the areal extents shown in Figures 2 and 4.

and negligible time scale for transport and storage) may not be valid. Depending on the case, ^{10}Be-derived erosion rates from disequilibrium landscapes may correctly quantify the mean erosion rate of an entire basin (Norton et al., 2008; Gudmundsdottir et al., 2013; Willenbring et al., 2013; Moon et al., 2018) or result in large variations that are not easily interpretable based on simple sediment mixing or topographic attributes (e.g., Binnie et al., 2007).

However, topographic analysis of channel and hillslope profiles and networks helps to assess whether landscapes are in topographic equilibrium and if these landscapes are influenced by network changes through divide migration or river capture (Whipple and Tucker, 1999; Willett et al., 2014; Yang et al., 2015; Beeson et al., 2017; Whipple et al., 2017; Simoes et al., 2021). In topographic equilibrium landscapes, it is expected that hillslopes and channels are coupled, and drainages have stable divides. The topographic metrics representing channel steepness and hillslope gradient show patterns similar to those of basin-averaged erosion rates. Recent studies have characterized river channel networks, drainage divide networks, and drainage divide geometry using various methods and assessed the potential of divide migration (Gilbert, 1877; Schwanghart and Scherler, 2014; Willett et al., 2014; Forte and Whipple, 2018). Perron and Royden (2013) developed an integral quantity, χ, based on drainage area to measure river geometry and network topology. Willett et al. (2014) showed that χ differences across a divide may imply drainage basin disequilibrium and a potential for divide migration. A study by Forte and Whipple (2018) expanded this idea of Gilbert (1877) and Willett et al. (2014) and presented a suite of topographic metrics, "Gilbert metrics," that quantify drainage-divide stability from headwater channel points. Scherler and Schwanghart (2020a, 2020b) recently proposed a method for extracting drainage divide networks and quantifying the relative magnitude and direction of divide migration based on hillslope relief differences. The across-divide differences in these topographic metrics can also be produced by other factors (e.g., rock erodibility, aspect, and surface material) without the divide migrating. Thus, by examining across-divide differences in both the topographic metrics and ^{10}Be-derived erosion rates, we can estimate whether a drainage divide may continue to migrate in the future.

Located along the restraining bend of the San Andreas Fault, the San Bernardino Mountains provide a natural landscape for examining how perturbations from active tectonics and drainage network reorganization develop transient landscapes and influence ^{10}Be-derived erosion rates (Figs. 1 and 2). East-west– and northwest-trending faults impose tectonic forcing on the landscape, which influences river incision and potentially induces changes in drainage networks and drainage divides. Previous studies showed that million-year and millennial-scale erosion rates, from low-temperature thermochronometry and cosmogenic radionuclides, respectively, are generally similar and increase from north to south across the San Bernardino Mountains, which suggests a dominant, first-order control from the tectonic uplift gradient (Spotila et al., 1998, 2001, 2002; Binnie et al., 2007, 2008, 2010; Fosdick and Blisniuk, 2018). However, Binnie et al. (2008) showed that tectonic blocks within the San Bernardino Mountains may have different stages of orogenesis and varying degrees of erosional and topographic equilibrium that produce different correspondences between million-year and millennial-scale erosion rates. Due to the limited spatial coverage of existing ^{10}Be-derived erosion-rate data and a lack of detailed topographic analysis, the effects of transient landscapes and river reorganizations on observed variations in ^{10}Be-derived erosion rates remain elusive.

Here, we test the hypothesis that ^{10}Be-derived erosion rates in the San Bernardino Mountains reflect topographic disequilibrium from perturbations by tectonic forcing and channel reorganization. If sediments are adequately mixed within a catchment, ^{10}Be-derived erosion rates may represent the averaged erosion rates of the entire basin although landscapes include topographic disequilibrium features. In addition, we expect that large differences in both erosion rates and topographic metrics across drainage divides occur in transient landscapes with divide migration.

To test this hypothesis, we expanded the spatial coverage of ^{10}Be-derived erosion rates, performed extensive topographic analysis to capture landscape transiency, and systematically compared ^{10}Be-derived erosion rates with disequilibrium landscape patterns. We identified the areas with topographic disequilibrium, such as decoupled channels and hillslopes, the presence of low-relief surfaces, longitudinal profile changes, and strong drainage-divide asymmetry. In these areas, we expect that the relationships among erosion rates and channel and hillslope metrics may be decoupled. ^{10}Be-derived erosion rates may correlate better with topographic metrics that capture the degree of topographic disequilibrium (e.g., areal extent of relict topography).

In addition, we expect across-divide differences in both topographic metrics and ^{10}Be-derived erosion rates with consistent directions of divide migration. Based on our results, we discuss the potential connections between divide asymmetry patterns and perturbations from fault activity and drainage reorganization in the evolving strike-slip restraining bend of the San Andreas Fault in the southern San Bernardino Mountains.

TECTONIC BACKGROUND

The restraining bend of the San Andreas Fault in southern California induces transpression that has resulted in the uplift of the Transverse Ranges for the past ~6 m.y. (Nicholson et al., 1994; Ingersoll and Rumelhart, 1999). Prior to uplift, the San Bernardino Mountains were continuous with the Mojave Desert to the north. Since then, the San Bernardino Mountains have uplifted along various east-west–trending faults of the San Andreas Fault system, exposing

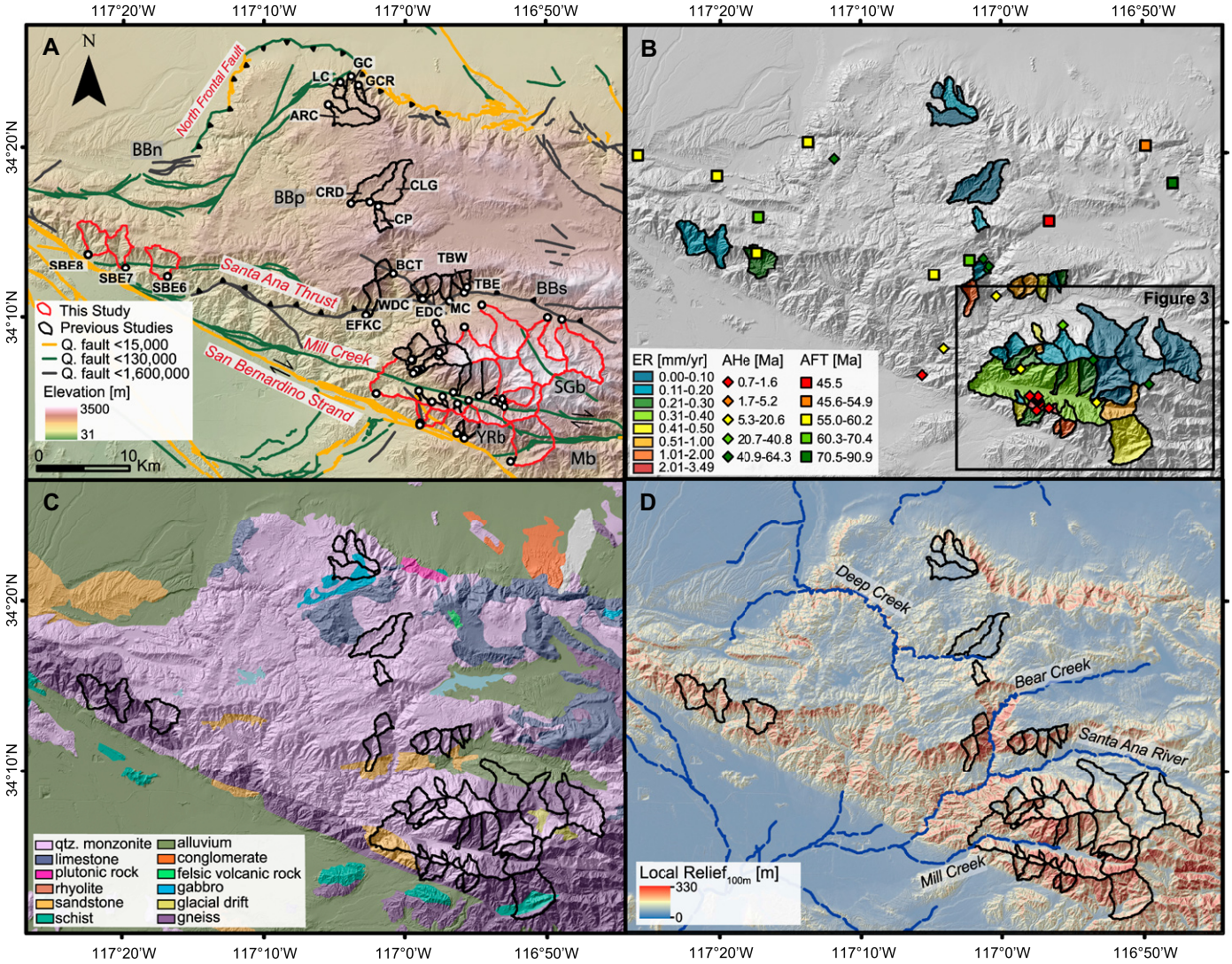

Figure 2. (A) Elevation map of the San Bernardino Mountains with Quaternary faults and sample names (black text in white boxes). Basins from this study and Binnie et al. (2006, 2007, 2008) are shown in red and black outlines, respectively. (B) Hillshade map with basins color-coded by ^{10}Be-derived erosion rate (ER, mm/yr) and locations of low-temperature thermochronologic samples color-coded by apatite (U-Th)/He ages (AHe ages, in Ma) and fission track ages (AFT; Blythe et al., 2002; Spotila et al., 1998, 2002). (C) Lithology map from Jennings et al. (1977). (D) Local relief map calculated using 100-m-radius circular window (local relief$_{100m}$); blue dashed lines indicate major rivers and creeks. In panel A, the locations of basins in the Big Bear block are shown with their sample names (also see San Gorgonio and Yucaipa Ridge blocks in Fig. 3). Quaternary faults (Q. fault) mapped by the U.S. Geological Survey are colored by fault activity <15,000 years (orange), <130,000 years (green), and <1,600,000 years (gray). The San Bernardino and Mill Creek strands of the San Andreas Fault, Santa Ana thrust, and North Frontal Fault are denoted. The tectonic blocks analyzed in this study are labeled as the northern (BBn) and southern (BBs) escarpments and plateau surface (BBp) of the Big Bear block, San Gorgonio block (SGb), Yucaipa Ridge block (YRb), and Morongo block (Mb).

deeply weathered granitic rocks in the high plateau area (Spotila et al., 1998; Fig. 2). Major faults divide the San Bernardino Mountains into several tectonic blocks, which include the Big Bear block, San Gorgonio block, Wilson Creek block (also referred to as Cram Peak by Kendrick et al., 2015), Yucaipa Ridge block, and Morongo block (Spotila et al., 1998; Fig. 3).

The tectonic blocks within the San Bernardino Mountains are separated by major east-west–trending active and inactive faults with variable geomorphic characteristics (Figs. 1 and 2A). The northernmost Big Bear block is bounded by two escarpments. The northern escarpment is formed by the inactive North Frontal thrust system, and the southern escarpment is formed by the inactive Santa Ana thrust. The Big Bear block is predominantly composed of quartz-monzonite and granodiorite (Jennings et al., 1977). The plateau surface has an average elevation of ~1900 m, up to ~2500 m at its peak, and contains outcrops of deeply weathered granitic rocks overlain with basalts and Miocene sediments (Oberlander, 1972).

The San Gorgonio block is south of the Big Bear block and is bounded by an unnamed high-angle fault in the north and the Mill Creek Fault to the south (Fig. 2A). Previous studies found that the Mill Creek Fault is inferred to be inactive based on the unfaulted sediment deposits at the Mill Creek Jumpoff (Matti et al., 1992; Kendrick et al., 2022; Fig. 2). The San Gorgonio block reaches an elevation of up to ~3500 m at

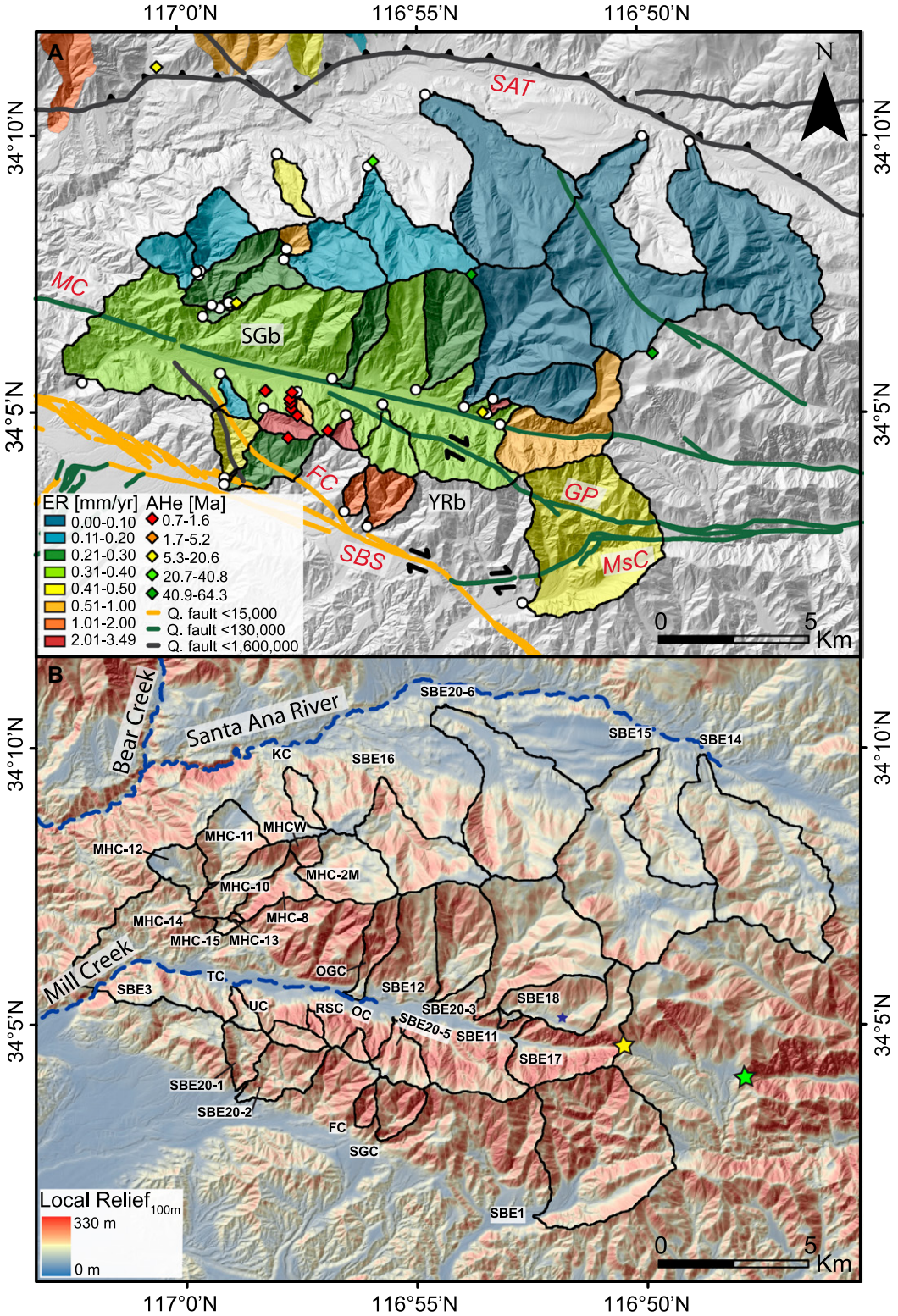

Figure 3. A close-up map of the San Gorgonio and Yucaipa Ridge blocks shows (A) erosion rates (ER, mm/yr) and apatite (U-Th)/He ages (AHe ages, in Ma) (Blythe et al., 2002; Spotila et al., 1998, 2001) and (B) local relief$_{100m}$ with sample names. In panel A, Quaternary faults (Q. fault) mapped by the U.S. Geological Survey are shown, with colors representing their times of last activity. Santa Ana thrust (SAT), Ford Canyon Fault (FC), and the Galena Peak (GP), San Bernardino (SBS), Mission Creek (MsC), and Mill Creek (MC) strands of the San Andreas Fault system are labeled. The oldest AHe ages are found at higher elevations within the San Gorgonio block (SGb) from relict topography. The youngest and fastest erosion occurs within the Yucaipa Ridge block (YRb). Adjusted erosion rates for the nested basin, within SBE11 outside of SBE18, are shown in panel A. Areas of low local relief in the upstream part of SGb in panel B have low erosion rates, which likely represent relict landscapes and topographic disequilibrium between hillslopes and channels. In panel B, the blue star indicates the location of the topographic bench above Mill Creek, the yellow star marks the location of the Mill Creek Jumpoff, and the green star indicates the location of the Middle Fork Jumpoff.

its center and has apatite helium ages of 55.7–52.6 Ma near its peak (Spotila et al., 1998). Similar ages have been found on the plateau surface, although the elevation is ~1 km lower than at the San Gorgonio block. The warped isochrons of apatite helium ages and the orientation of weathered granite surface exposures indicate that the San Gorgonio block may be a gentle antiform with high local uplift in its center and ~10° northward, 2° eastward, and 5.5° westward tilting (Sadler and Reeder, 1983; Spotila et al., 1998). Steep slopes in the south are composed of granitic and gneissic rocks (Jennings et al., 1977).

The Yucaipa Ridge and Morongo blocks are south of the San Gorgonio block (Fig. 2A). Both the Yucaipa Ridge and Morongo blocks are composed of gneissic and granodioritic rocks

(Morton et al., 2008) and have steep, rugged topography. The Yucaipa Ridge block has a narrow width (~3 km) and consists of a complex fault network including the Mill Creek Fault in the north, the San Bernardino and Mission Creek strands of the San Andreas Fault system in the south, and the Ford Canyon Fault within it (Kendrick et al., 2015; Beyer et al., 2018). The Yucaipa Ridge block reaches elevations of up to ~2800 m near the ridge top and has young apatite helium ages of 1.6–0.7 Ma, which indicate >3–4 km of exhumation over the past few million years (Spotila et al., 1998). The Morongo block is southeast of the Yucaipa Ridge block and is bounded by the San Bernardino strand of the San Andreas Fault in the northwest, the Mission Creek Fault in the northeast, the thrust and reverse faults of the San Gorgonio Pass Fault zone in the south, and the Whitewater Fault in the east (Spotila et al., 1998; Kendrick et al., 2022). The Morongo block reaches elevations of up to ~2400 m and has older apatite helium ages than the Yucaipa Ridge block of 5.2–4.5 Ma at elevations of 1000 m, which indicates ~0.4 mm/yr of exhumation over the past few million years (Spotila et al., 2002). Kendrick et al. (2022) subdivided the Morongo block into two blocks, the Kitching Peak block on the east and the Pisgah Peak blocks on the west, separated by the San Bernardino strand of the San Andreas Fault.

PREVIOUS WORK: EROSION RATES IN THE SAN BERNARDINO MOUNTAINS

Previous studies measured million-year and millennial-scale erosion rates using low-temperature thermochronometry and cosmogenic radionuclides, respectively, from the San Bernardino Mountains (Spotila et al., 1998, 2002; Blythe et al., 2000, 2002; Binnie et al., 2006, 2007). Spotila et al. (2002) inferred million-year erosion rates from apatite (U-Th)/He ages, assuming a closure temperature of 70 °C, a geothermal gradient of 30 °C/km, and a surface temperature of 10 °C (Wright, 1991). Both apatite (U-Th)/He ages and ^{10}Be-derived erosion rates suggest that million-year and millennial-scale erosion rates increase from north (0.04–0.1 mm/yr and 0.05–0.13 mm/yr, respectively) to south (0.17–1.2 mm/yr and 0.95–1.5 mm/yr, respectively) across the San Bernardino Mountains (Figs. 1 and 2; Spotila et al., 2002; Binnie et al., 2008). The spatially consistent, southward-increasing pattern of erosion rates at different time scales suggests that tectonic uplift rates and topographic development control overall erosion rates (Binnie et al., 2008). However, relative magnitudes of million-year and millennial-scale erosion rates vary depending on tectonic blocks, likely representing different stages of orogenesis and various mechanisms (Binnie et al., 2008).

In the northern San Bernardino Mountains, the Big Bear block has an extensive pre-uplift, low-relief plateau with low erosion rates and exhibits early-stage orogenesis (Spotila et al., 1998; Binnie et al., 2008). Within the southern escarpment of the Big Bear block, ^{10}Be-derived erosion rates are ~4 times higher than million-year erosion rates and generally increase with topographic slopes. The increased erosion rates in recent times are consistent with an interpretation that the southern escarpment is a transient landscape with ongoing headward erosion and drainage reorganization (Spotila et al., 2002; Binnie et al., 2008). In addition, ^{10}Be-derived erosion rates are especially high near the heavily incised Bear Creek in the southern escarpment (Fig. 2B; ~1.37 mm/yr in sample EFKC; Spotila et al., 2002; Binnie et al., 2008). Bear Creek is currently incising into the plateau after capturing a part of the Deep Creek basin around 1.5 m.y. ago that drained toward the northwestern portion of the Big Bear block (Cox et al., 2003). This inference is supported by observations that both drainages have similar elevations near the channel head and geographic alignments (Spotila et al., 2002).

In the San Gorgonio block, which has a limited extent of pre-uplift surfaces, ^{10}Be-derived erosion rates are ~1.5 times higher than million-year erosion rates. In the Yucaipa Ridge block, the averages of million-year and millennial-scale erosion rates from the Yucaipa Ridge block are similarly high (~1.5 mm/yr). ^{10}Be-derived erosion rates from the Yucaipa Ridge block vary by about a factor of three but with similarly steep hillslope gradients, indicating a threshold topography of actively uplifting mountains (Binnie et al., 2008). Appreciable variations in ^{10}Be-derived erosion rates in the southern San Bernardino Mountains have been attributed to disequilibrium landscapes, incomplete mixing of sediments, and inputs from stochastic events such as landslides (Binnie et al., 2006, 2008). In summary, although tectonic uplift rates are considered to be the first-order control on ^{10}Be-derived erosion rates across the San Bernardino Mountains, previous studies have identified the potential influence of disequilibrium landscapes on ^{10}Be-derived erosion rates in certain areas (Spotila et al., 2002; Binnie et al., 2006, 2008) that can be further examined with additional ^{10}Be-derived erosion rate data and detailed topographic analysis.

METHODS

^{10}Be-Derived Erosion Rates

We calculated millennial-scale erosion rates using measurements of in situ-produced ^{10}Be-derived erosion rates in quartz mineral grains from detrital sands from 16 small (2.2–18.1 km^2) basins and one large (108.9 km^2) basin in the San Bernardino Mountains (Fig. 2). We collected three samples following an approximate west-east transect along the southern escarpment, eight samples on both sides of the divide of the San Gorgonio block, four samples from the Yucaipa Ridge block, and two samples from basins extending across the southern San Gorgonio block and northern Yucaipa Ridge block (Fig. 2). Two sets of 12 and five samples were collected and analyzed in 2018–2019 and 2019–2020, respectively (Table S1 in the Supplemental Material[1]).

We first processed detrital sand samples in the University of California, Los Angeles (UCLA) Cosmogenic Radionuclide Sample Preparatory Laboratory, where we sieved them to the 250–710 μm fraction. We then separated quartz using magnetic separation, a 50% HNO_3 bath with deionized (DI) water, heavy liquid density separation, and several stages of acid leaching with a ~1% HNO_3 and ~1% hydrofluoric acid (HF) mixture with DI water. We measured the purity of each quartz separate using inductively coupled plasma–optical emission spectrometry at the National Science Foundation/University of Vermont Community Cosmogenic Facility (NSF/UVM CCF). Following quartz separation, we extracted pure Be from the quartz at the NSF/UVM CCF using the methods described in Corbett et al. (2016). We prepared samples in two separate batches, each of which included one blank and one quality control standard. We added ~250 μg of Be as carrier to ~20 g of purified quartz, using two different Be carriers for the two sample batches (prepared in 2018 and 2019; Supplemental Text S1). We digested the samples in concentrated HF and processed them through anion exchange columns and cation exchange columns to separate Be. We precipitated the Be fractions as hydroxide gels, combusted to BeO, mixed with Nb, and packed them into stainless steel cathodes for measurement by accelerator mass spectrometry.

The ^{10}Be/^{9}Be ratios were measured at the Center for Accelerator Mass Spectrometry at Lawrence Livermore National Laboratory. The ratios were normalized against the standard 07KNSTD3110 with an assumed ratio of 2.85×10^{-12} (Nishiizumi et al., 2007). Because

[1]Supplemental Material. Text to explain blank corrections for ^{10}Be data and the influence of drainage area on erosion rates, tables, and additional figures to supplement the main text are included in the Supplemental Material. Please visit https://doi.org/10.1130/GSAB.S.23638794 to access the Supplemental Material, and contact editing@geosociety.org with any questions.

we used two different Be carriers, we applied different blank corrections to the two batches (Supplemental Text S1).

We calculated erosion rates using the Lal/Stone time-dependent production model based on the measured concentrations of ^{10}Be (Lal, 1991; Stone, 2000) and an assumed rock density of 2.6 g/cm^3 using the CRONUS-Earth online calculator version 3.0 (Balco et al., 2008). We calculated the topographic metrics required for erosion calculations such as basin-averaged latitude, longitude, and elevation using TopoToolbox v2 in Matlab (Schwanghart and Scherler, 2014; Table S2).

In addition, we compiled and recalculated 31 basin-averaged, ^{10}Be-derived erosion rates from previous studies (Binnie et al., 2006, 2007, 2008; Table S3), which resulted in a total of 48 basins in the San Bernardino Mountains. Recalculation was necessary to standardize for the same ^{10}Be half-life (Nishiizumi et al., 2007), production-rate scaling schemes of the Lal/Stone time-dependent production model (Lal, 1991; Stone, 2000), and rock density (2.6 g/cm^3). Although some previous studies excluded basins with an area of <1 km^2 due to potential biases in small basins from recent landslides (DiBiase et al., 2010), we included those basins in our analysis for consistency with previous studies from the San Bernardino Mountains (Binnie et al., 2007). We then examined the biases of erosion rates due to drainage basin areas and their influence on our results (Supplemental Text S2).

Near the Mill Creek Fault, we have one pair of nested basins: a "parent" basin, SBE11, and a nested sub-basin, SBE18. Following the approach from Portenga et al. (2015), we calculated the effective erosion rate of SBE11 for the non-nested portion that lies outside of the nested sub-basin SBE18:

$$\textit{Effective erosion rate} = \frac{\left(\begin{array}{l}\textit{Parent basin erosion flux}\\ -\textit{Sub-basin erosion flux}\end{array}\right)}{\left(\begin{array}{l}\textit{Parent basin area}\\ -\textit{Sub-basin area}\end{array}\right)}. \quad (1)$$

This effective erosion rate for the non-nested sub-basin will improve interpretations of the spatial distribution of local erosion rates. We included the effective erosion rate for the sub-basin in Table S1.

Topographic Analysis

We performed topographic analysis using a U.S. Geological Survey (USGS) National Elevation Dataset 1/3 arc-second (~10 m) digital elevation model (DEM) (https://earthexplorer.usgs.gov/) and TopoToolbox v2 (Schwanghart and Scherler, 2014). We analyzed the topographic metrics for channel and hillslope, which include profile geometry and plan-view networks. We also calculated channel steepness, hillslope gradient, local relief, and area percentages of low-relief surfaces to quantify the degrees of topographic variation across the San Bernardino Mountains (Table S2). Then, we quantified the profiles and network of rivers and drainage divides and assessed the topographic asymmetries across drainage divides.

Channel Steepness, Hillslope Gradient, and Topographic Relief

We calculated the normalized channel steepness (k_{sn}) to analyze the longitudinal profiles of channels. We first extracted channel points with drainage areas larger than 0.1 km^2. Then, we calculated the channel steepness k_s from the relationship between elevation z and χ using the integral method (Perron and Royden, 2013):

$$z(x) = z(x_b) + \left(\frac{k_s}{A_0{}^{\theta}}\right)\chi, \quad \text{with}$$
$$\chi = \int_{x_b}^{x}\left(\frac{A_0}{A(x)}\right)^{\theta} dx, \quad (2)$$

where x is a horizontal distance (m) from a base-level position, x_b; z is an elevation (m); θ is a concavity; A_0 is a reference drainage area (m^2); and k_s is channel steepness. χ is calculated based on the spatial integration of drainage area from a certain base level to a headwater. The linear trend between z and χ is relatable with k_s. Deviations from this linear trend imply transient evolution of a river profile or heterogeneous environmental factors (e.g., rock edibility and sediments). We determined basin-averaged k_{sn} assuming $A_0 = 0.1$ km^2 and a reference concavity of 0.45. We assumed reference concavity of 0.45 to be consistent with a previous study by DiBiase et al. (2010), and a base elevation of 1100 m—i.e., $z(x_b)$—to be consistent with that of Forte and Whipple (2018).

We calculated hillslope gradient as the steepest descent gradient in an eight-cell neighborhood. Local relief was calculated as the elevation difference between the highest and lowest elevations within a certain radius of a circular window across the region. We used different length scales of circular windows, 100 m and 1500 m, to capture the relief related to different landforms, hillslopes, and channels, respectively. These length scales generally correspond to lengths of hillslope spacing and fluvial valley widths in our study areas. However, this size window is approximate, and measurements may not be accurately captured in certain locations, especially in fluvial valleys that are too narrow (e.g., Yucaipa Ridge block). Hereafter, the length scale of relief (i.e., the radius of the circular window) is shown as a subscript for local relief (e.g., local relief$_{100m}$ and local relief$_{1500m}$).

We calculated an area percentage of low-relief surface within a basin to capture the areal extent of pre-uplift, low-relief surface in the upland region and calculated this as the percentage of basin area that has a value of local relief$_{100m}$ of <70 m. The threshold of 70 m was determined based on average local relief$_{100m}$ values of the gentle upland surface identified in Figure 3B.

River and Divide Networks and Divide Asymmetry

We examined channel and divide networks and divide migration potential within the tectonic blocks of the San Bernardino Mountains using topographic metrics from headwater channel points and hillslope relief across the divides (Fig. 4). First, we calculated Gilbert metrics, including χ, elevation, local relief, and gradient following the approach of Forte and Whipple (2018) at headwater channel locations. The headwater points for each basin were determined to be the upstream portion that has a minimum accumulation area of 0.1 km^2. For the χ calculation, we used a reference area of 0.1 km^2 and a base elevation of 1400 m (Willett et al., 2014; Forte and Whipple, 2018). We used local relief calculated as an elevation range within a circular window with a radius of 500 m, and obtained channel elevation and hillslope gradient from a 10-m-resolution DEM. We extracted elevation, χ, local relief, and hillslope gradient at headwater channel locations from two basins that share the divide. Generally, the divide will move in the direction of low relief or gradient and high elevation or χ.

Second, we calculated the divide asymmetry index (DAI) to infer the relative magnitude and direction of divide migration based on hillslope relief across the divide (Scherler and Schwanghart, 2020a) using divide asymmetry functions in TopoToolbox v2 (Scherler and Schwanghart, 2020a). This tool defines drainage divides as lines that delineate the margins of drainage basins and quantifies their networks based on determined endpoints, segments, and junctions. The endpoints are where drainage basin boundaries start or end, and the junctions are where three or more divide segments meet. The divide segments are then sorted to create the branching drainage divide network, similar to a stream network. DAI is calculated as hillslope relief differences from the divide to the nearest channel head normalized by the sum of hillslope relief

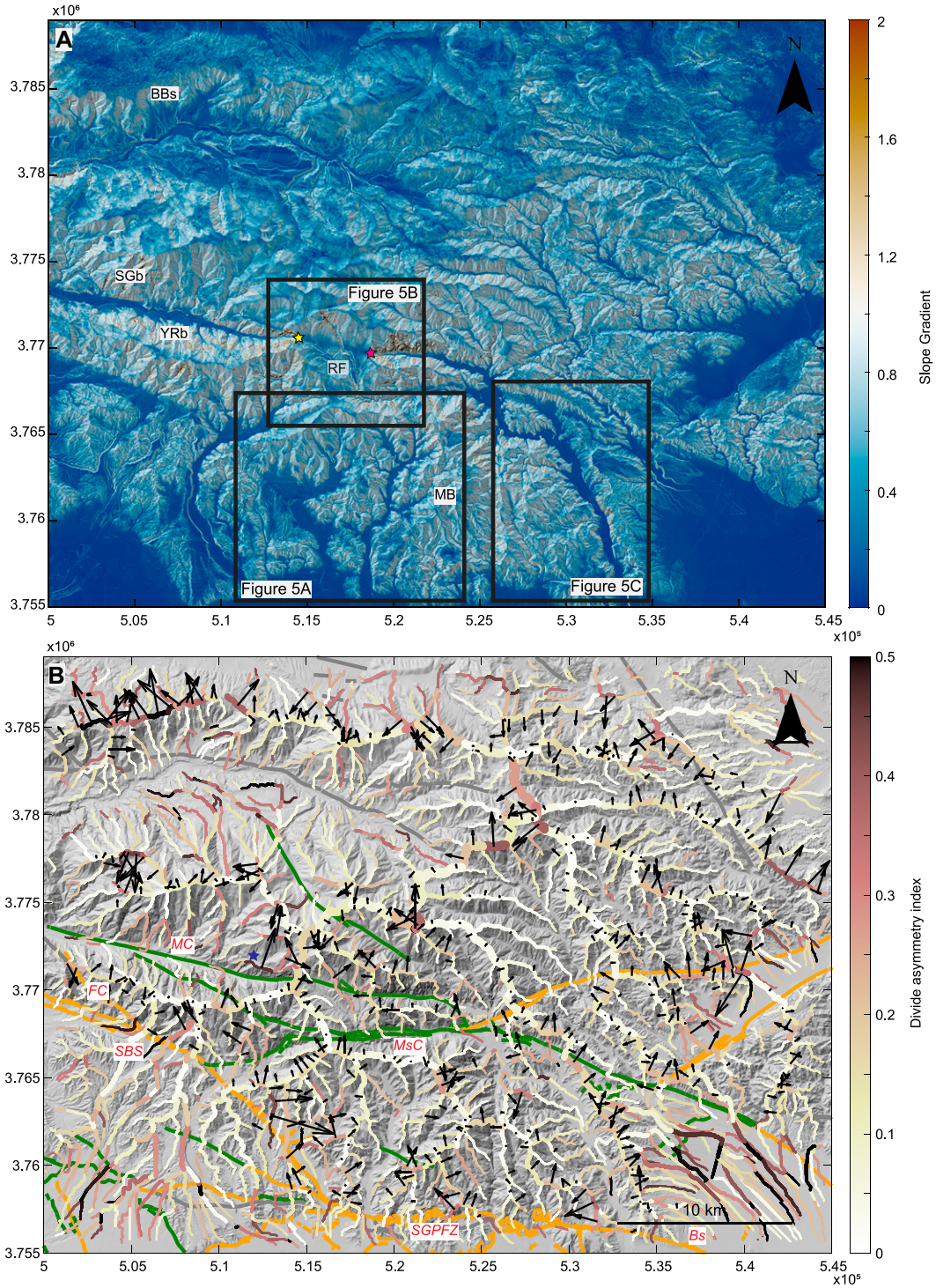

Figure 4. (A) Hillslope gradient map based on the 10-m-resolution digital elevation model (DEM) of the U.S. Geological Survey (USGS) National Elevation Dataset (https://earthexplorer.usgs.gov/) and (B) divide asymmetry index map of the southern San Bernardino Mountains. The yellow star in panel A is the location of the Mill Creek Jumpoff, and the pink star is the location of the Middle Fork Jumpoff. Areas of interest enlarged in Figures 5A, 5B, and 5C are shown in boxes. In panel A, the tectonic blocks and areas of interests are labeled as southern escarpments of the Big Bear block (BBs), San Gorgonio block (SGb), Yucaipa Ridge block (YRb), Morongo block (MB), and Raywood Flat area (RF). In panel B, the magnitudes and directions of black arrows represent the magnitude of the average divide asymmetry index and direction of divide migration (e.g., lower hillslope relief), respectively. Quaternary faults (Q. fault) mapped by the USGS are shown with colors representing their last activities: <15,000 years (orange), <130,000 years (green), and <1,600,000 years (gray). The Ford Canyon Fault (FC), San Gorgonio Pass Fault zone (SGPFZ), and San Bernardino (SBS), Mission Creek (MsC), Mill Creek (MC), and Banning (Bs) strands of the San Andreas Fault system are labeled. Maps are shown in the WGS84 UTM 11N coordinate.

on both sides of the divide. DAI can vary from 0 (symmetric) to 1 (most asymmetric). We calculated the DAI along the divide segments of tectonic blocks of the San Bernardino Mountains (Figs. 4 and 5). The magnitudes and orientations of arrows shown in Figures 4 and 5 represent the magnitudes of DAI and the direction of divide migration (i.e., lower hillslope relief), respectively.

Comparison between Basin-Averaged Erosion Rates and Controls

To assess the controls of ^{10}Be-derived erosion rates, we compared the ^{10}Be-derived erosion rates for all 48 basins from the San Bernardino Mountains to their basin-averaged values of topographic metrics, mean annual precipitation, and distance to the San Andreas Fault. We examined topographic metrics including k_{sn}, slope, local relief$_{100m}$, and local relief$_{1500m}$. We obtained mean annual precipitation rates (MAP, in mm/yr) from 800 m-resolution annual precipitation rates averaged over 30 years covering 1991–2020 (PRISM data set from https://prism.oregonstate.edu). We calculated the distance to the active San Andreas Fault (Dist$_f$) as the shortest horizontal distance between basin pixels and

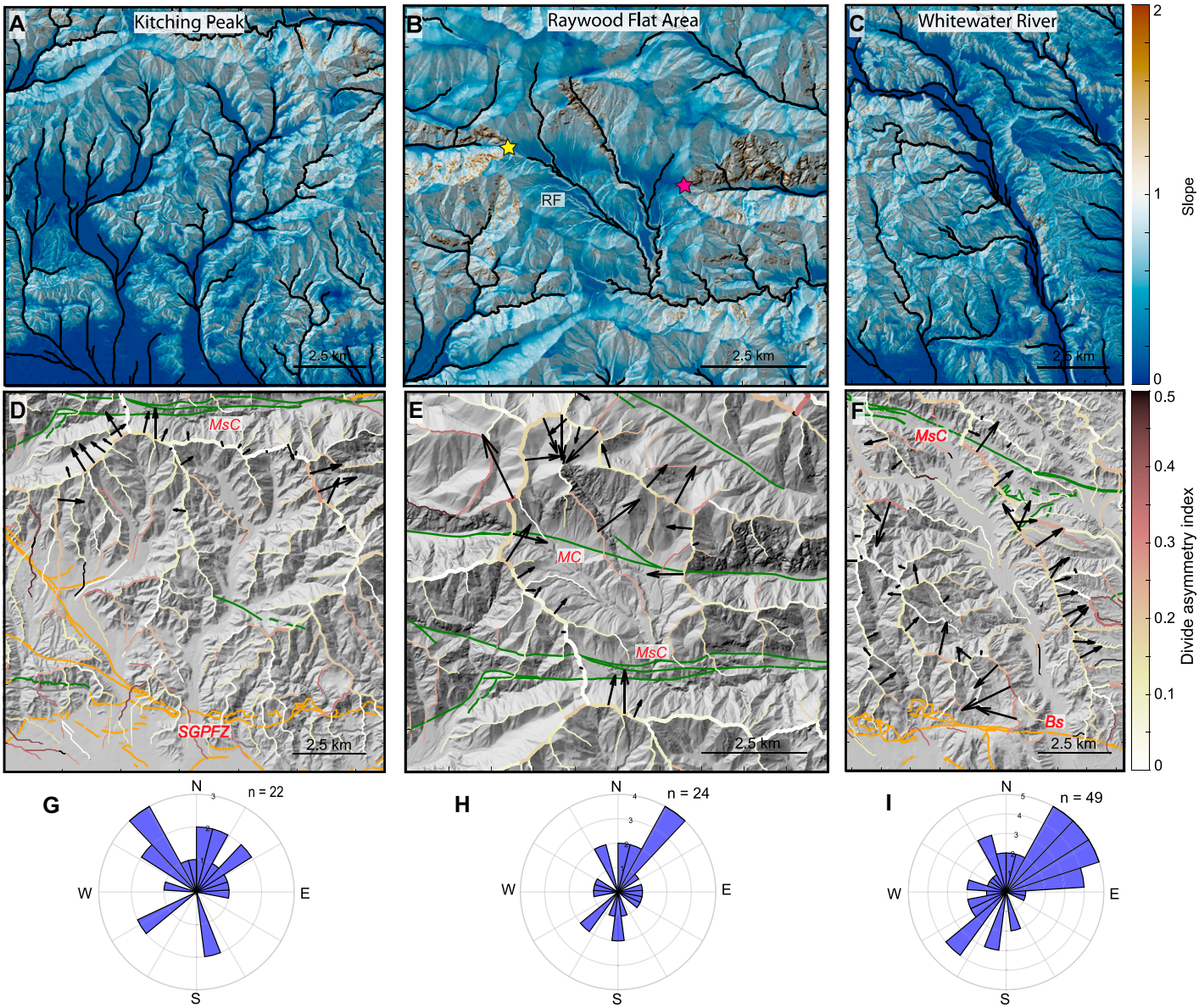

Figure 5. Maps of (A–C) slope, (D–F) divide asymmetry index, and (G–I) rose diagrams for divide migration direction for (A, D, G) Kitching Peak, (B, E, H) the drainage covering the Raywood Flat (RF) area, and (C, F, I) Whitewater River. The divide asymmetry index in Kitching Peak suggests strong northwestward divide migration in the western ridgeline, potentially due to the structural or lithologic controls from the south. Divides around the Raywood Flat region migrate in encroaching directions, likely due to fault inactivity of the Mill Creek (MC) and Mission Creek (MsC) strands. Western and eastern divides along the downstream section of the of Whitewater River migrate to the northeast or southwest, respectively, indicating basin expansions potentially related to the river capture. The San Gorgonio Pass Fault zone (SGPFZ) and Banning (Bs) strands of the San Andreas Fault system are also labeled.

the San Andreas Fault mapped as the Holocene and historically active by the U.S. Geological Survey (U.S. Geological Survey, Quaternary fault and fold database for the United States, accessed 1 May 2021: https://www.usgs.gov/natural-hazards/earthquake-hazards/faults).

We examined the correlations between ^{10}Be-derived erosion rates and their controls based on linear ($y = n_1 + n_2x$), nonlinear power-law ($y = b_1x^{b_2}$), and monotonic relationships. Y is the ^{10}Be-derived erosion rate, x are the controls (e.g., topographic metrics), and n_1, n_2, b_1, and b_2 are the best-fit parameters. To assess the goodness of fit, we calculated root mean square error (RMSE) as the square root of the sum of squared errors divided by the degrees of freedom. For monotonic relationships, we calculated Spearman's rank correlation coefficient and p-values. Lower RMSE and higher Spearman's rank correlation coefficient imply a better fit. The correlation coefficients and p-values were calculated for basins from all individual tectonic blocks of the San Bernardino Mountains (Table S4).

We examined eight paired basins across divides, five pairs in the San Gorgonio block, and three pairs in the Yucaipa Ridge block to assess potential divide migration. To provide a robust assessment, we used three methods based on differences in erosion rates and topography. First, we compared the differences in erosion

rates of basins that share a divide (Fig. 3). We compared the 2σ range of erosion rates from each paired basin. If they overlapped within the 2σ range, we predicted that the divide was stable. If they did not overlap, we predicted that the divide would migrate toward the direction of the basin with a lower erosion rate. Second, we calculated the mean values of Gilbert metrics from headwater channel points, including χ, elevation, local relief, and gradient within our paired basins. We tested the statistical differences between Gilbert metrics from each side using either (1) *t*-tests with a *p*-value of 0.05 or (2) 1σ standard deviation range following the approach of Forte and Whipple (2018). The divide is predicted to migrate in the direction of the basin with the higher χ, higher elevation, lower relief, or lower gradient at channel head points. Lastly, we examined the magnitudes of DAI in the shared divide segment, which is based on hillslope relief across the divide. A divide is predicted to migrate in the direction of the lower hillslope relief.

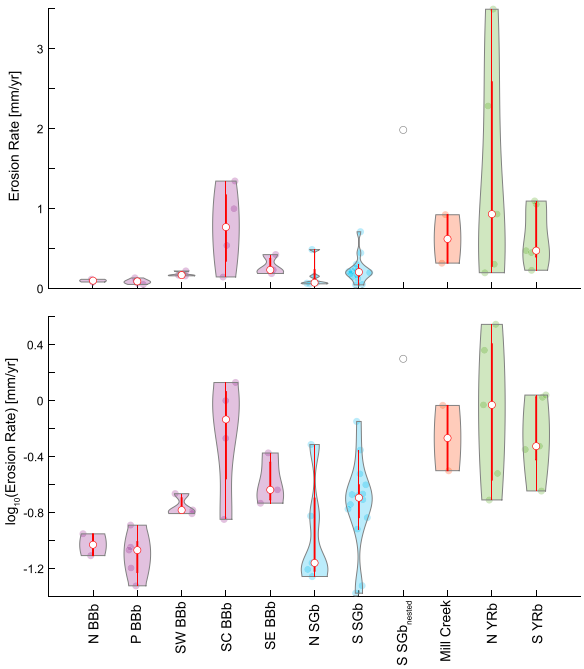

Figure 6. Probability distributions of erosion rates for subsections of three major tectonic blocks of the San Bernardino Mountains are shown using violin plots in linear scale (top) and log scale (bottom). The white circle within the violin plot is the median. The thick red lines are the box plot, with the top and bottom indicating the 25th and 75th percentiles and the whiskers (thinner red lines) indicating the 99.3% range. The thickness of the violin plot indicates the relative abundance of the data points in the y axis. The violin plots are color-coded by tectonic block: Big Bear block (purple, BBb), San Gorgonio block (blue, SGb), Mill Creek basins overlapping southern San Gorgonio Block and northern Yucaipa Ridge block (orange, Mill Creek), and Yucaipa Ridge block (green, YRb). N—north; P—plateau; SW—southwest; SC—south-central; SE—southeast. Erosion rate of one nested basin in S SGb is shown as S SGb_{nested}. This nested basin with steep slopes and high channel steepness has a high erosion rate that is similar to the basins of the N YRb. Samples from the SC Big Bear block tend to have high erosion rates compared to other sections of the Big Bear block.

RESULTS

Erosion Rate Ranges and Distributions within and across Tectonic Blocks

Our new and recalculated ^{10}Be-derived erosion rates range from 0.04 ± 0.003 to 3.04 ± 0.56 mm/yr within the San Bernardino Mountains (Tables S1 and S3; Figs. 2 and 3). As in previous studies (Binnie et al., 2006, 2007, 2008, 2010), we observed a general, southward-increasing trend of ^{10}Be-derived erosion rates from the Big Bear block in the north (0.05–1.37 mm/yr, 0.30 ± 0.37, n = 17; hereafter, the minimum to maximum range, mean ± 1σ range, and the number of samples are shown) to the Yucaipa Ridge block in the south (0.20–3.04 mm/yr, 1.04 ± 0.91 mm/yr, n = 10; Fig. 6). Generally, Big Bear block erosion rates are the lowest within the San Bernardino Mountains.

Our compilation of new and previously examined samples shows appreciable differences across the southern escarpment, including east-west variations. ^{10}Be-derived erosion rates along the southern escarpment (0.15–1.37 mm/yr, 0.46 ± 0.43 mm/yr, n = 10) are higher than those of the northern escarpment (0.08–0.09 mm/yr, 0.09 ± 0.01 mm/yr, n = 2) or the plateau surface (Fig. 6; 0.05–0.13 mm/yr, 0.09 ± 0.03 mm/yr, n = 5). The southern escarpment was split into three portions for more detailed analyses: the southwest, south-central, and southeast escarpments. ^{10}Be-derived erosion rates from the south-central escarpment (0.15–1.37 mm/yr, 0.79 ± 0.54 mm/yr, n = 4) adjacent to Bear Creek are higher than those from the southwestern (0.16–0.22 mm/yr, 0.18 ± 0.03 mm/yr, n = 3) and southeastern (0.19–0.43 mm/yr, 0.29 ± 0.13 mm/yr, n = 3) escarpments. Hillslopes along the southern escarpment are close to the threshold hillslope gradient (0.5–0.6, dimensionless), but the basin-average $relief_{1500m}$ and k_{sn} are higher in the south-central escarpment (920 ± 57 m, and 122 ± 18 $m^{0.9}$, respectively, n = 4) than in the southwest (762 ± 49 m and 97 ± 11 $m^{0.9}$, n = 3) and southeast (751 ± 22 m and 103 ± 16 $m^{0.9}$, n = 3) escarpments. Although our new measurements from the southwestern escarpment are closer to the active San Andreas Fault, the highest erosion rate is found near Bear Creek Canyon, the most heavily incised channel in the south-central escarpment of the plateau surface (Fig. 2).

We also observed varying ^{10}Be-derived erosion rates from east to west and from north to south across the divide in the southern San Bernardino Mountains (Fig. 6). The erosion rates from the San Gorgonio block are slightly lower in the northern part (0.06–0.50 mm/yr, 0.17 ± 0.19 mm/yr, n = 5) than in the southern part (0.04–0.76 mm/yr, 0.24 ± 0.18 mm/yr, n = 14), and generally lower in the western part (0.04–0.15 mm/yr, 0.070 ± 0.038 mm/yr, n = 6) than in the eastern part (0.12–0.76 mm/yr, 0.29 ± 0.18 mm/yr, n = 13). However, the Yucaipa Ridge block has a wide range of erosion rates (0.20–3.04 mm/yr, 1.62 ± 1.42 mm/yr, n = 10), and two basins with very high erosion rates (>2.0 mm/yr) are located on the northwestern side. The high values of erosion rates in the Yucaipa Ridge block are consistent when we consider erosion rates only from basins with drainage area >1 km^2 (0.26–2.12 mm/yr, 1.19 ± 0.93 mm/yr, n = 6). Although basins of the San Gorgonio block generally have lower erosion rates than those of the Yucaipa Ridge block, high erosion rates are observed from the headwater of Mill Creek (0.99 mm/yr, SBE17) and the nested basin of SBE11 (2.1 mm/yr) along the eastern Mill Creek (Fig. 3).

Erosion Rates versus Controls across the Tectonic Blocks

^{10}Be-derived erosion rates from the San Bernardino Mountains show statistically significant positive relationships with slope, $relief_{100m}$, $relief_{1500m}$, and k_{sn}, and weak negative relationships with $Dist_f$ (Figs. 7, S1, and S2; Table S4). However, the trends and strengths of correlations among erosion rate and controls differ for

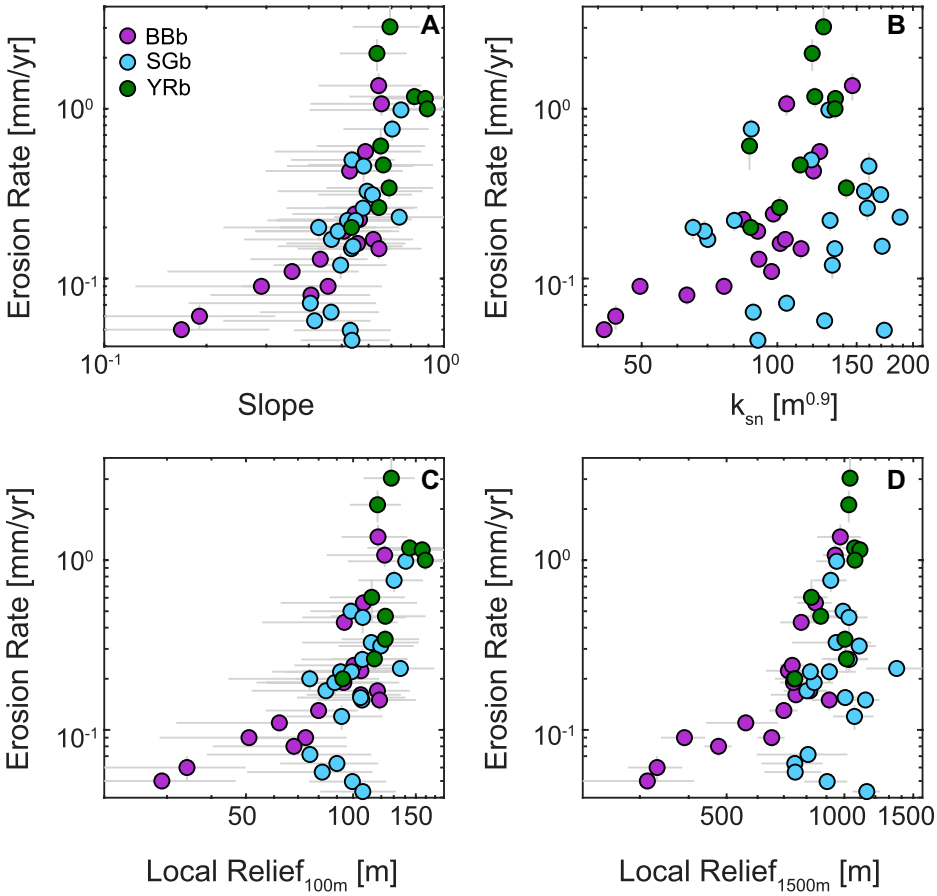

Figure 7. Scatter plots showing log-scale relationships between ^{10}Be-derived erosion rate (mm/yr) and (A) slope, (B) $k_{sn}(m^{0.9})$, (C) local relief$_{100m}$(m), and (D) local relief$_{1500m}$(m). Light gray error bars show one standard deviation, except for k_{sn}, with one standard error. Basins sampled from the Big Bear block (BBb), San Gorgonio block (SGb), and Yucaipa Ridge block (YRb) are shown in purple, light blue, and green, respectively. Some samples from SGb in panels B and D show a trend that deviates from the overall trends of BBb and YRb.

each tectonic block. For basins of the Big Bear block, erosion rates show good correlations to k_{sn} ($R^2 = 0.66$, power law), slope ($R^2 = 0.50$, power law), and local relief$_{100m}$ and local relief$_{1500m}$ ($R^2 = 0.43$ and 0.50, respectively, power law). Erosion rates from the San Gorgonio block show poor correlations with local relief$_{1500m}$ ($R^2 = 0.02$, power law) and k_{sn} ($R^2 = 0.004$, power law), although they have good correlations with topographic metrics measured over smaller length scales, such as slope ($R^2 = 0.56$, power law), and local relief$_{100m}$ ($R^2 = 0.52$, power law; Figs. 7B, 7D, and S1). Some erosion rates from the San Gorgonio block visually appear to deviate from the trend of increasing erosion rates with increasing topographic metrics, especially for k_{sn} and local relief$_{1500m}$ (Figs. 7B, 7D, and S1). Although erosion rates appear to increase with increases in topographic metrics within the Yucaipa Ridge block (Fig. 7), there are no statistical correlations to topographic metrics (Table S4), which is likely due to the threshold topography (Binnie et al., 2007, 2008).

Although there is some scatter in the relationship between erosion rates and area percentages of low relief, basins with higher percentages of low relief surface generally tend to have lower erosion rates (Figs. 8 and 9). However, some samples from the eastern portion of the San Gorgonio block (e.g., SBE14, SBE15, SBE18, SBE20-3, and SBE20-06) tend to have much lower erosion rates than expected from trends with topographic metrics, including area percentages of low relief, local relief, and k_{sn} (dark blue in Fig. 9).

In summary, basins across the San Bernardino Mountains show that erosion rates increase with increasing slope, k_{sn}, and local relief$_{1500m}$, and decreasing percentage of low-relief topography. The basins in the northern escarpment and plateau surface have low erosion rates, low k_{sn} and local relief$_{1500m}$, and a high percentage of low-relief topography, while the southern escarpments of the Big Bear block and Yucaipa Ridge block generally have high erosion rates, high k_{sn} and local relief$_{1500m}$, and a low percentage of low-relief topography. However, some San Gorgonio block samples tend to have low erosion rates and a high percentage of low-relief topography despite the high k_{sn} and local relief$_{1500m}$. Erosion rates have statistically significant, weak negative correlations with the distance to the mapped active San Andreas Fault ($R^2 = 0.14$, power law). The negative correlations may be due to high erosion rates from basins close to southern blocks near the southern San Andreas Fault. Erosion rates from the San Bernardino Mountains show no statistically significant correlation with modern MAP rates. These overall results are consistent regardless of including or excluding basins smaller than 1 km^2 (Supplemental Text S1; Figure S2; Table S4).

Divide Migration Patterns in the Tectonic Blocks

Divide migration patterns inferred from across-divide differences in erosion rates, Gilbert metrics, and divide asymmetry index (DAI) show different degrees of consistency depending on their locations within and across the tectonic blocks (Fig. 4, Table S5). Along the southern escarpment, DAI values are generally high (>0.25). Both DAI and headwater channel topographic metrics consistently indicate that the divide is migrating into the plateau surface.

For the San Gorgonio block, we investigated the migration of the east-west–trending divide using five N-S–draining paired basins (Figs. 3A and 4; Table S5). Within the western portion of the San Gorgonio block, two pairs of basins (MHC-2 M and OGC; SBE16 and SBE12) consistently indicate the possibility of northward divide migration based on erosion rates, Gilbert metrics, and DAI values of ~0.20. In the eastern portion of the San Gorgonio block, divide migration interpretations become inconsistent. SBE20-3 shares a divide with two basins, SBE20-6 and SBE15, to the northwest and northeast, respectively. The migration direction from erosion rates, Gilbert metrics, and DAI on the eastern portion of the San Gorgonio block are mostly stable or show alternating directions (Fig. 4). Although there are no paired basins for confirmation, some basins with high erosion rates in the San Gorgonio block tend to have high DAI values in their divides. There are very high DAI values (>0.4) near the nested sub-basin of SBE11 in a steep erosional bedrock scarp

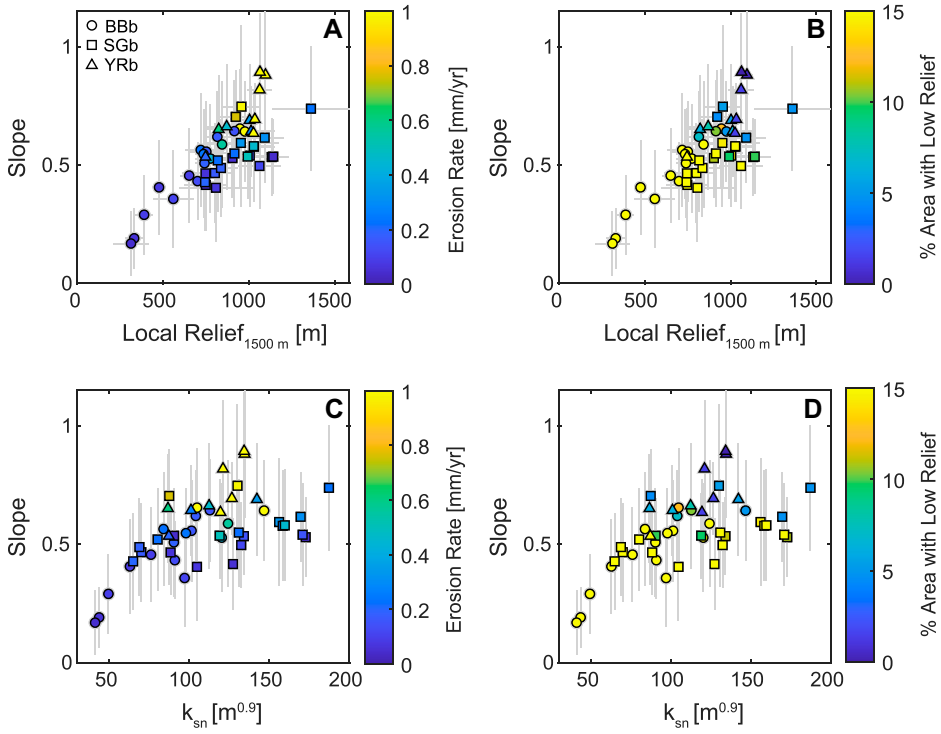

Figure 8. Scatter plots showing relationships between slope and (A, B) local relief$_{1500m}$(m) and (C, D) channel steepness (k_{sn}(m$^{0.9}$)) for samples from tectonic blocks of the San Bernardino Mountains. Symbol colors represent ^{10}Be-derived erosion rates in panels A and C and the percentage of basin area with local relief$_{100m}$ less than 70 m (i.e., % area with low relief) in panels B and D. Light gray error bars show one standard deviation, except for k_{sn} with one standard error. Basins sampled from the Big Bear block (BBb), San Gorgonio block (SGb), and Yucaipa Ridge block (YRb) are shown in circles, squares, and triangles, respectively. Some samples from the SGb deviated from the generally positive relationships between slope and local relief and slope and k_{sn}. These samples with low slope, high local relief, and high k_{sn} tend to have low erosion rates and areas with a high percentage of low local relief. These samples are mostly from the eastern SGb, with topographic disequilibrium between the downstream channels and upland relict surface.

boundary and a headwater basin that feeds Mill Creek (SBE17). This indicates that the increased erosion rates may drive divide migration and consume the surrounding drainage basins.

We examine the divide migration of the east-to-west–trending drainage divide based on three N-S–draining paired basins in the Yucaipa Ridge block (Fig. 3A; Table S5). The western pair (TC and SBE20-1) and eastern pair (SBE20-5 and SGC) suggest potential northward migration based on differences in erosion rate and DAI. However, Gilbert metrics show inconsistent results. The pair in the middle, UC and SBE202, suggests the possibility of migration toward the south based on erosion rate. Conversely, DAI and most of the Gilbert metrics suggest the potential for northward migration. The magnitude of DAI divide migration in the Yucaipa Ridge block is generally small (~0.05), indicating stable divides (Fig. 4).

DISCUSSION

Erosional Patterns across the San Bernardino Mountains

Our compilation of new and previously examined measurements of ^{10}Be-derived erosion rates across the San Bernardino Mountain blocks show a southward-increasing trend, similar to previous studies (Binnie et al., 2007, 2008, 2010). Analysis and comparison of ^{10}Be-derived erosion rates from individual basins and their potential controls suggest that topographic metrics produce stronger controls on ^{10}Be-derived erosion rates compared to the distance to mapped active fault or MAP (Table S4; Fig. S2). Binnie et al. (2010) also found no relationship between modern MAP and ^{10}Be-derived erosion rates in three basins from the remnants of pre-uplift weathered surfaces despite a factor of three difference in MAP. However, both topographic steepness and MAP generally increase toward the south (Spotila et al., 2002). In addition, we have limited information on past climatic history and have not examined the influences of distributions, frequency, and magnitudes of intense precipitation on sediment transport and erosion (e.g., DiBiase et al., 2012). Thus, we cannot rule out the subordinate influences of precipitation rates on erosion rates and erosional mechanisms in the region.

Our new measurements with extended spatial coverage and topographic analyses reveal three distinct patterns of ^{10}Be-derived erosion rates and highlight the potential influences from disequilibrium landscapes. First, our results suggest that the increased erosion rates within the central portion of the southern escarpment are due to transient landscapes driven by channel reorganization and not the proximity to the mapped active San Andreas Fault. Our new rates from the southwestern escarpment are lower than erosion rates around Bear Creek in the central portion of the southern escarpment (Fig. 2). Erosion rates are locally high near the heavily incised Bear Creek channel and are lower to the west and east away from Bear Creek. Channel profile analysis along the main stream of the Santa Ana River shows that there is one major knickpoint ~18 km upstream of the confluence of Bear Creek (Fig. S3). The basin that incorporates the knickpoint along the southern escarpment has the highest ^{10}Be-derived erosion rate (1.37 mm/yr, sample EFKC). Generally, samples surrounding Bear Creek, and those in close proximity to the knickpoint, also have higher erosion rates (0.14–0.56 mm/yr, n = 3). This is consistent with increased incision after the Santa Ana River captured Bear Creek, which may have once flowed to the north as part of the Deep Creek basin (Spotila et al., 2002).

Basins from the western southern escarpment have relatively high precipitation rates (MAP of ~873 mm/yr) and likely have undergone recent base level changes due to the active San Andreas Fault (Spotila et al., 2002). However, our observed erosion rates are similar to those of the eastern southern escarpment but lower than those from the central portion. We find that these low erosion rates from the western and eastern southern escarpment are consistent with similarly low local relief$_{1500m}$ and lower k_{sn}. This pattern suggests that crustal uplift and overall topography may control erosion rates here (Binnie et al., 2010).

Second, we find that ^{10}Be-derived erosion rates from the southern San Bernardino Mountains may reflect variations from increased tectonic uplift to the south and local perturbation from topographic disequilibrium induced by

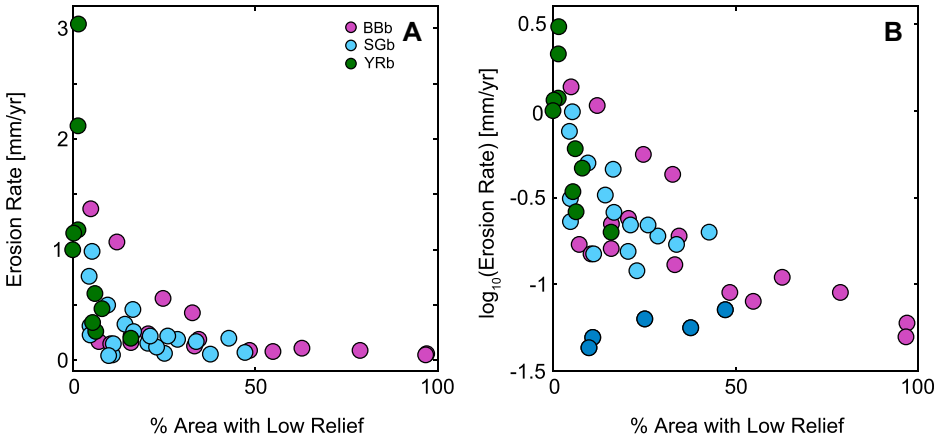

Figure 9. Plot showing erosion rate against the area percentage with low relief (% area with low relief) in (A) linear and (B) log scale. The % area with low relief is calculated as a percentage of basin area that has the value of local relief$_{100m}$ < 70 m. Basins sampled from the Big Bear block (BBb), the San Gorgonio block (SGb), and the Yucaipa Ridge block (YRb) are shown in purple, light blue, and green, respectively. Generally, basins with higher erosion rates have a lower percentage of area with low relief. Outliers from the SGb (dark blue, SBE18, SBE20-3, SBE14, SBE15, and SBE20-6, from left to right) show much lower erosion rates for a given percentage of the basin area with low relief.

active tectonics and river incision. Although low-relief surfaces on the San Gorgonio block are not as extensive as on the plateau surface, some basins from the San Gorgonio block have a relatively large area that incorporates these low-relief surfaces unlike at the Yucaipa Ridge block. The presence of relict surfaces in the San Gorgonio block suggests that the landscapes are in topographic disequilibrium and actively changing over time. For example, basins draining from the top of the central San Gorgonio block, such as SBE20-3 and SBE20-6, have high k_{sn} and large-scale local relief due to the steep downstream sections. We expect these basins to have undergone locally high channel incision. However, we find that the basin-averaged ^{10}Be-derived erosion rates are low, which is consistent with low hillslope gradient and local relief$_{100m}$. This pattern is likely due to the influence of relict surfaces and gentle upland areas. Topographic metrics that are small in length-scale, such as hillslope gradient and local relief$_{100m}$, and the area percentages of low-relief topography, tend to better characterize these topographic features than the large length-scale topographic metrics of k_{sn} and local relief$_{1500m}$.

However, some of the eastern San Gorgonio block samples (dark blue basins in Fig. 9) have lower-than-expected erosion rates in comparison to other samples with similar percentages of low-relief topography. This indicates that assumptions for ^{10}Be-derived erosion rates (e.g., well-mixed sediment) may not be valid in these basins, and there is a potential for sediment input with very high ^{10}Be concentrations. Sediment with high ^{10}Be concentrations may come from the weathering of relict, heavily weathered bedrock at the ridgeline, sediments from ancient drainages (Spotila et al., 2002), or mapped deposits from past glaciations along the ridgeline of the eastern San Gorgonio block (Owen et al., 2003; Fig. 3). The exposure ages from boulders in the crests of glacial moraines were dated at 5–20 ka and had ^{10}Be concentrations of 10^6–10^7 atoms/g (Owen et al., 2003), which are higher than those of our samples from the eastern San Gorgonio block.

Lastly, we find that erosion rates along the restraining bend may be locally high due to influences from tectonic or geomorphic events to which the basins are still responding. We find that some basins in the southern portion of the San Gorgonio block, such as SBE20-3 and SBE17 in the east, have a knickpoint with a large elevation drop (e.g., ~21 m). These are part of a ~2-km-long flat bench above a steep step along Mill Creek (Fig. 3), where the Mill Creek Fault is currently considered inactive (Matti et al., 1992; Weldon, 2010; Kendrick et al., 2015, 2022). The divide beneath the flat bench indicates a strong northward migration. This flat bench may be the result of base-level change due to either a past slip event along the Mill Creek Fault or geomorphic events, such as debris flows. Debris flows from the headwaters or tributaries of Mill Creek may scour the downstream channel. Although the San Gorgonio block has generally low erosion rates, the erosion rates from this steep section (~2.1 mm/yr) and the headwater of Mill Creek (~0.99 mm/yr) are high, as are the DAI values (>0.2). These locally high erosion rates in the San Gorgonio block are comparable to the erosion rates observed in the Yucaipa Ridge block, with higher tectonic uplift rates. We suggest that these erosion rate signals could reflect not only overall tectonic uplift patterns, but also disequilibrium landscapes driven by ongoing changes in tectonics and river networks within an active and evolving strike-slip restraining bend.

Divide Migration and Erosion Patterns within the Southern San Bernardino Mountains

Our combined analysis of erosion rates from paired samples and topographic analysis provides a tool for assessing the divide migration potential in locations of the southern San Bernardino Mountains. DAI shows the northward migration along the divide of the southern escarpment, likely due to the Santa Ana River incising into the plateau surface, which is consistent with previous interpretations (Binnie et al., 2008; Forte and Whipple, 2018). However, across the divides of the San Gorgonio and Yucaipa Ridge blocks, our divide migration assessments from erosion rates and topographic metrics (e.g., divide asymmetry index) show different results depending on location (Table S5).

In the San Gorgonio block, the two basin pairs in the west suggest possible northward migration while two basin pairs in the east indicate generally stable divides. The western San Gorgonio block tends to have steep slopes and lower fractions of low-relief topography compared to those in the eastern San Gorgonio block. Previous studies suggest that the Mill Creek Fault has been inactive since at least 100 ka (Matti et al., 1992; Weldon, 2010; Kendrick et al., 2015, 2022).

However, recent studies suggest potential slip along certain segments of the Mission Creek Fault (Fosdick and Blisniuk, 2018; Blisniuk et al., 2021). Previous studies suggest that fault slip is transferred from an inactive, eastern segment of the Mill and Mission Creek faults to the more recently active Galena Peak Fault or unmapped strands of the Mission Creek Fault along left steps near the boundary of the southeastern portion of the Yucaipa Ridge block (Fosdick and Blisniuk, 2018; Figs. 3 and 4A). These fault strands may eventually connect to the western San Bernardino strand of the San Andreas Fault (Blisniuk et al., 2021; McGill et al., 2021). Due to the change in fault activity near the eastern segment of the Mill Creek Fault, this region may still be responding to tectonic forcing and further from steady-state topography, which could be causing locally high erosion rates (e.g., SBE11 and SBE17). It is possible that the active

western segment of Mill Creek produces higher incision and more pronounced northward divide migrations than in the east.

Divide migration analysis within the Yucaipa Ridge block is mostly inconclusive. Some DAI along the Yucaipa Ridge block support a northward migration, potentially driven by a relatively more active southern San Bernardino strand compared to the Mill Creek strand. However, the magnitudes of DAI are relatively small in the Yucaipa Ridge block (~0.05) compared to DAI in the southern escarpment (~0.25) and the San Gorgonio block (~0.15) (Fig. 4). In addition, the divide migration directions are not consistent according to the differences in erosion rates and Gilbert metrics from the three basin pairs (Table S5). This inconclusive divide migration pattern is consistent with the interpretation that the narrow Yucaipa Ridge block is likely at threshold topography and rapidly incising on both sides in response to active tectonics (Binnie et al., 2008).

Our assessments of topographic metrics (e.g., DAI) show potential northward migrations across the divides of the southern escarpment and western San Gorgonio block, and our results suggest influences from northward escarpment retreat along the southern escarpment and perturbations either from river reorganization (e.g., capture) or fault activity (e.g., more active fault in the south) in the San Gorgonio block. We found that erosion rates in steep landscapes of the San Bernardino Mountains can be locally high due to geomorphic changes or events without the involvement of tectonic forcing. It is also possible that other factors, such as processes related to aspect (e.g., south-facing slopes) or inherited structural form, may contribute to erosion processes and observed topographic asymmetry. For example, the structural shape of the San Gorgonio block from past northward and westward tilting may contribute to the overall geomorphic form (Spotila et al., 1998) rather than active tectonics. Thus, we need to cautiously interpret ^{10}Be-derived erosion-rate measurements to infer tectonic uplift rates and consider the influences from transient landscape evolution in certain areas of the San Bernardino Mountains.

Potential Connection among Fault Activity, River Capture, and Divide Migration

In previous sections, we showed that perturbations by tectonic forcing and channel reorganization can induce divide migration and influence ^{10}Be-derived erosion rates in some areas of the San Bernardino Mountains. We now apply divide asymmetry analysis at other locations along the restraining bend of the southern San Andreas Fault. We focus on the southernmost San Bernardino Mountains, especially for areas where ^{10}Be-derived erosion rate data are not available, such as the Morongo block (Figs. 4 and 5). Analysis of divide asymmetry at these locations can be used to identify areas with topographic disequilibrium and provide insights into perturbation from slip transfer or river capture. We examined the landforms and divide migration patterns using hillslope gradient and DAI of the Kitching Peak, Raywood Flat near Mill Creek Jumpoff, and Whitewater River areas in the Morongo block. In these areas, the locations of currently active fault segments or the landscape evolution scenarios are heavily debated (Matti et al., 1992; Weldon, 2010; Kendrick et al., 2015, 2022; Fosdick and Blisniuk, 2018; Blisniuk et al., 2021).

First, divide migration patterns in the Kitching Peak area indicate that topographic disequilibrium in this area may be related to more active faults in the south. Kitching Peak is located directly south of the inactive Mission Creek strand, east of the active Banning strand of the San Andreas Fault, and north of the reverse and thrust faults of the San Gorgonio Pass Fault zone (Figs. 5A and 5D). The hillslope in this region appears to be well dissected, with minimal low-relief upland areas (Fig. 5A). The magnitude of DAI is generally high near the active faults, and the dominant orientations of divide migration are northeast or northwest (Figs. 5D and 5G). Consistent northwest migration is predicted along the E-W–oriented divides just south of mapped, inactive Mission Creek. Interestingly, the downstream portion of these channels seems to have NE-SW–oriented deflection or offset, which may indicate potential influences from unmapped structures or lithologic variations. The predominantly northward divide migrations and overall steep threshold slopes in this area would suggest that the perturbations from active faults and ongoing channel reorganization in the south may drive northward divide migration and contribute to the topographic development.

Second, divide migration patterns in the Raywood Flat area indicate a shrinking drainage basin, likely due to fault inactivity. The Raywood Flat area, east of the Mill Creek Jumpoff and west of the Middle Fork Jumpoff, has the inactive Mill Creek strand in the center and the inactive Mission Creek in the south. The Raywood Flat area has distinctively gentle hillslopes (Fig. 5B). Additionally, the orientations of divide migrations indicate that this basin is encroaching inward and will be consumed or captured by surrounding drainages (Figs. 5E and 5H). If the Mill Creek and Mission Creek faults had more recent fault activity, we would expect sharper slopes adjacent to the faults and expanding drainage basins with outward divide migration.

Lastly, the divide migration patterns in the Whitewater River region are likely due to river capture from the south. In this region, the divides of tributaries joining the downstream Whitewater River migrate predominantly northwest or northeast, away from the main Whitewater River (Figs. 5F and 5I). This indicates that the Whitewater River is incising into the surrounding areas, including surfaces of Mission Creek alluvial fans and fanglomerates. Thus, Mission Creek may have previously flowed eastward along the fault and deposited these alluvial fans until it was captured by the Whitewater River (Fosdick and Blisniuk, 2018). Owen et al. (2014) and Balco et al. (2019) dated these Mission Creek alluvial fans and fanglomerates, respectively, and showed that their ages range from > marine isotope stage 4 (>57 ka) to ca. 260 ka. The exact timings and durations of the river-capture event were unclear, but the fans have been beheaded by Whitewater River. This suggests that the capture likely occurred after 57 ka. The divide migration patterns are consistent with landscape changes caused by this geologically recent river-capture event.

CONCLUSIONS

Our work shows that the spatial variations of millennial-scale, ^{10}Be-derived erosion rates from 17 newly sampled and 31 compiled basins in the San Bernardino Mountains generally reflect an erosional response to the activity of range-bounding faults and have some influences from a lagged response in hillslopes from rivers incising into the blocks. ^{10}Be-derived erosion rates show an overall southward-increasing trend, reflecting the influence of the tectonic uplift gradient that is consistent with previous studies.

However, we also observe appreciable variations in ^{10}Be-derived erosion rates across the San Bernardino Mountains, which are related to landscape transiency. Along the southern escarpment, we observed erosion rate variations, with the highest erosion rates found in the middle of the escarpment surrounding a deeply incised channel that resulted from a river-capture event. Erosion rates within the southern blocks of the San Bernardino Mountains (i.e., San Gorgonio and Yucaipa Ridge blocks) are generally high compared to those from the Big Bear block, reflecting higher tectonic uplift rates proximal to the active restraining bend of the San Andreas Fault. Yet, erosion rates from the San Gorgonio block reflect influences from the presence of relict topography and the potential of divide migration in the western portion. Within the Yucaipa Ridge block, divide migration patterns are inconsistent, likely due to the establishment

of threshold topography from high tectonic uplift rates and rapid river incision.

We also present examples of divide migration patterns in the Morongo block, which may indicate the potential influences of perturbations from fault activity, slip transfer, or river captures and reorganization. Overall, we suggest that ^{10}Be-derived erosion rates along strike-slip restraining bends in the San Bernardino Mountains may reflect not only overall long-term tectonic uplift patterns, but also the influence of transient landscape response (e.g., river incision, hillslope, and river network) induced by different activities of range-bounding faults or ongoing channel reorganizations.

ACKNOWLEDGMENTS

We thank James Spotila, two anonymous reviewers, and the associate editor, E. Gabet, for constructive reviews. We thank S. Saha, J. Lin, R. Missel, and A. Richard for help with sampling, and G. Hilley, A. Neely, and J. Higa for discussions. This work was supported by National Science Foundation EAR-1945431 and 2012073 for S. Moon, 1806629 for N.D. Brown, 1848547 for K. Blisniuk, and 1735676 for the University of Vermont/National Science Foundation Community Cosmogenic Facility. This work was performed partly under the auspices of the U.S. Department of Energy by the Lawrence Livermore National Laboratory under contract DE-AC52-07NA27344; this manuscript is LLNL-JRNL-830450.

REFERENCES CITED

Baden, C.W., Shuster, D.L., Aron, F., Fosdick, J.C., Bürgmann, R., and Hilley, G.E., 2022, Bridging earthquakes and mountain building in the Santa Cruz Mountains, CA: Science Advances, v. 8, https://doi.org/10.1126/sciadv.abi6031.

Balco, G., Stone, J.O., Lifton, N.A., and Dunai, T.J., 2008, A complete and easily accessible means of calculating surface exposure ages or erosion rates from ^{10}Be and ^{26}Al measurements: Quaternary Geochronology, v. 3, p. 174–195, https://doi.org/10.1016/j.quageo.2007.12.001.

Balco, G., Blisniuk, K., and Hidy, A., 2019, Chlorine-36/beryllium-10 burial dating of alluvial fan sediments associated with the Mission Creek strand of the San Andreas Fault system, California, USA: Geochronology, v. 1, p. 1–16, https://doi.org/10.5194/gchron-1-1-2019.

Beeson, H.W., McCoy, S.W., and Keen-Zebert, A., 2017, Geometric disequilibrium of river basins produces long-lived transient landscapes: Earth and Planetary Science Letters, v. 475, p. 34–43, https://doi.org/10.1016/j.epsl.2017.07.010.

Behr, W.M., Rood, D.H., Fletcher, K.E., Guzman, N., Finkel, R., Hanks, T.C., Hudnut, K.W., Kendrick, K.J., Platt, J.P., and Sharp, W.D., 2010, Uncertainties in slip-rate estimates for the Mission Creek strand of the southern San Andreas Fault at Biskra Palms Oasis, southern California: Geological Society of America Bulletin, v. 122, p. 1360–1377, https://doi.org/10.1130/B30020.1.

Beyer, J., Cooke, M.L., and Marshall, S.T., 2018, Sensitivity of deformation to activity along the Mill Creek and Mission Creek strands of the southern San Andreas Fault: Geosphere, v. 14, p. 2296–2310, https://doi.org/10.1130/GES01666.1.

Binnie, S.A., Phillips, W.M., Summerfield, M.A., and Fifield, L.K., 2006, Sediment mixing and basin-wide cosmogenic nuclide analysis in rapidly eroding mountainous environments: Quaternary Geochronology, v. 1, p. 4–14, https://doi.org/10.1016/j.quageo.2006.06.013.

Binnie, S.A., Phillips, W.M., Summerfield, M.A., and Fifield, L.K., 2007, Tectonic uplift, threshold hillslopes, and denudation rates in a developing mountain range: Geology, v. 35, p. 743–746, https://doi.org/10.1130/G23641A.1.

Binnie, S.A., Phillips, W.M., Summerfield, M.A., Fifield, L.K., and Spotila, J.A., 2008, Patterns of denudation through time in the San Bernardino Mountains, California: Implications for early-stage orogenesis: Earth and Planetary Science Letters, v. 276, p. 62–72, https://doi.org/10.1016/j.epsl.2008.09.008.

Binnie, S.A., Phillips, W.M., Summerfield, M.A., Fifield, L.K., and Spotila, J.A., 2010, Tectonic and climatic controls of denudation rates in active orogens: The San Bernardino Mountains, California: Geomorphology, v. 118, p. 249–261, https://doi.org/10.1016/j.geomorph.2010.01.005.

Blisniuk, K., Rockwell, T., Owen, L.A., Oskin, M., Lippincott, C., Caffee, M.W., and Dortch, J., 2010, Late Quaternary slip rate gradient defined using high-resolution topography and ^{10}Be dating of offset landforms on the southern San Jacinto Fault zone, California: Journal of Geophysical Research: Solid Earth, v. 115.

Blisniuk, K., Oskin, M., Mériaux, A., Rockwell, T., Finkel, R.C., and Ryerson, F.J., 2013, Stable, rapid rate of slip since inception of the San Jacinto Fault, California: Geophysical Research Letters, v. 40, p. 4209–4213, https://doi.org/10.1002/grl.50819.

Blisniuk, K., Scharer, K., Sharp, W.D., Burgmann, R., Amos, C., and Rymer, M., 2021, A revised position for the primary strand of the Pleistocene-Holocene San Andreas Fault in southern California: Science Advances, v. 7, https://doi.org/10.1126/sciadv.aaz5691.

Blythe, A.E., Burbank, D.W., Farley, K.A., and Fielding, E.J., 2000, Structural and topographic evolution of the central Transverse Ranges, California, from apatite fission-track, (U-Th)/He and digital elevation model analyses: Basin Research, v. 12, p. 97–114, https://doi.org/10.1046/j.1365-2117.2000.00116.x.

Blythe, A.E., House, M.A., Spotila, J.A., and Barth, A., 2002, Low-temperature thermochronology of the San Gabriel and San Bernardino Mountains, southern California: Constraining structural evolution, *in* Barth, A., ed., Contributions to Crustal Evolution of the Southwestern United States: Geological Society of America Special Paper 365, p. 231–250, https://doi.org/10.1130/0-8137-2365-5.231.

Cochran, W.J., Spotila, J.A., Prince, P.S., and McAleer, R.J., 2017, Rapid exhumation of Cretaceous arc-rocks along the Blue Mountains restraining bend of the Enriquillo-Plantain Garden Fault, Jamaica, using thermochronometry from multiple closure systems: Tectonophysics, v. 721, p. 292–309, https://doi.org/10.1016/j.tecto.2017.09.021.

Collett, C.M., Duvall, A.R., Flowers, R.M., Tucker, G.E., and Upton, P., 2019, The timing and style of oblique deformation within New Zealand's Kaikōura Ranges and Marlborough Fault System based on low-temperature thermochronology: Tectonics, v. 38, p. 1250–1272, https://doi.org/10.1029/2018TC005268.

Cooke, M.L., and Dair, L.C., 2011, Simulating the recent evolution of the southern big bend of the San Andreas Fault, Southern California: Journal of Geophysical Research: Solid Earth, v. 116.

Corbett, L.B., Bierman, P.R., and Rood, D.H., 2016, An approach for optimizing in situ cosmogenic ^{10}Be sample preparation: Quaternary Geochronology, v. 33, p. 24–34, https://doi.org/10.1016/j.quageo.2016.02.001.

Cox, B.F., Hillhouse, J.W., and Owen, L.A., 2003, Pliocene and Pleistocene evolution of the Mojave River, and associated tectonic development of the Transverse Ranges and Mojave Desert, based on borehole stratigraphy studies and mapping of landforms and sediments near Victorville, California, *in* Enzel, Y., Wells, S.G., and Lancaster, N., eds., Paleoenvironments and Paleohydrology of the Mojave and Southern Great Basin Deserts: Geological Society of America Special Paper 368, p. 1–42, https://doi.org/10.1130/0-8137-2368-X.1.

Cunningham, W.D., and Mann, P., 2007, Tectonics of strike-slip restraining and releasing bends, *in* Cunningham, W.D., and Mann, P., eds., Tectonics of Strike-Slip Restraining and Releasing Bends: Geological Society, London, Special Publication 290, p. 1–12, https://doi.org/10.1144/SP290.1.

Dascher-Cousineau, K., Finnegan, N.J., and Brodsky, E.E., 2021, The life span of fault-crossing channels: Science, v. 373, p. 204–207, https://doi.org/10.1126/science.abf2320.

DiBiase, R.A., Whipple, K.X., Heimsath, A.M., and Ouimet, W.B., 2010, Landscape form and millennial erosion rates in the San Gabriel Mountains, CA: Earth and Planetary Science Letters, v. 289, p. 134–144, https://doi.org/10.1016/j.epsl.2009.10.036.

DiBiase, R.A., Heimsath, A.M., and Whipple, K.X., 2012, Hillslope response to tectonic forcing in threshold landscapes: Earth Surface Processes and Landforms, v. 37, p. 855–865, https://doi.org/10.1002/esp.3205.

Duvall, A.R., and Tucker, G.E., 2015, Dynamic ridges and valleys in a strike-slip environment: Journal of Geophysical Research: Earth Surface, v. 120, p. 2016–2026, https://doi.org/10.1002/2015JF003618.

Duvall, A.R., Harbert, S.A., Upton, P., Tucker, G.E., Flowers, R.M., and Collett, C., 2020, River patterns reveal two stages of landscape evolution at an oblique convergent margin, Marlborough Fault System, New Zealand: Earth Surface Dynamics, v. 8, p. 177–194, https://doi.org/10.5194/esurf-8-177-2020.

Forte, A.M., and Whipple, K.X., 2018, Criteria and tools for determining drainage divide stability: Earth and Planetary Science Letters, v. 493, p. 102–117, https://doi.org/10.1016/j.epsl.2018.04.026.

Fosdick, J.C., and Blisniuk, K., 2018, Sedimentary signals of recent faulting along an old strand of the San Andreas Fault, USA: Scientific Reports, v. 8, 12132, https://doi.org/10.1038/s41598-018-30622-3.

Gilbert, G.K., 1877, Geology of the Henry Mountains: Washington, D.C., Government Printing Office, https://doi.org/10.5962/bhl.title.51652.

Gudmundsdottir, M.H., Blisniuk, K., Ebert, Y., Levine, N.M., Rood, D.H., Wilson, A., and Hilley, G.E., 2013, Restraining bend tectonics in the Santa Cruz Mountains, California, imaged using ^{10}Be concentrations in river sands: Geology, v. 41, p. 843–846, https://doi.org/10.1130/G33970.1.

Ingersoll, R.V., and Rumelhart, P.E., 1999, Three-stage evolution of the Los Angeles basin, southern California: Geology, v. 27, p. 593–596, https://doi.org/10.1130/0091-7613(1999)027<0593:TSEOTL>2.3.CO;2.

Jennings, C.W., Strand, R.G., Rogers, T.H., Boylan, R.T., Moar, R.R., and Switzer, R.A., 1977, Geologic map of California: California Geological Survey Geologic Data Map 2.

Kendrick, K.J., Matti, J.C., and Mahan, S.A., 2015, Late Quaternary slip history of the Mill Creek strand of the San Andreas Fault in San Gorgonio Pass, southern California: The role of a subsidiary left-lateral fault in strand switching: Geological Society of America Bulletin, v. 127, p. 825–849, https://doi.org/10.1130/B31101.1.

Kendrick, K.J., Matti, J.C., and Barth, N.C., 2022, Geologic and geomorphic evidence for multi-phase history of strands of the San Andreas Fault through the San Gorgonio Pass structural knot, southern California: Geosphere, v. 18, p. 424–457, https://doi.org/10.1130/GES02424.1.

Lal, D., 1991, Cosmic ray labeling of erosion surfaces: In situ nuclide production rates and erosion models: Earth and Planetary Science Letters, v. 104, p. 424–439, https://doi.org/10.1016/0012-821X(91)90220-C.

Matti, J.C., and Morton, D.M., 1993, Paleogeographic evolution of the San Andreas Fault in southern California: A reconstruction based on a new cross-fault correlation, *in* Powell, R.E., Weldon, R.J., II, and Matti, J.C., eds., The San Andreas Fault System: Displacement, Palinspastic Reconstruction: Geological Society of America Memoir 178, p. 107–160, https://doi.org/10.1130/MEM178-p107.

Matti, J.C., Morton, D.M., and Cox, B.F., 1992, The San Andreas Fault system in the vicinity of the central Transverse Ranges province, southern California: U.S. Geological Survey Open-File Report 92-354, 49 p., https://doi.org/10.3133/ofr92354.

McGill, S.F., Owen, L.A., Weldon, R.J., and Kendrick, K.J., 2013, Latest Pleistocene and Holocene slip rate for the San Bernardino strand of the San Andreas Fault, Plunge Creek, Southern California: Implications for strain partitioning within the southern San Andreas

Fault system for the last ~35 ky: Geological Society of America Bulletin, v. 125, p. 48–72, https://doi.org/10.1130/B30647.1.

McGill, S.F., Owen, L.A., Weldon, R.J., Kendrick, K.J., and Burgette, R.J., 2021, Latest Quaternary slip rates of the San Bernardino strand of the San Andreas Fault, southern California, from Cajon Creek to Badger Canyon: Geosphere, v. 17, p. 1354–1381, https://doi.org/10.1130/GES02231.1.

Moon, S., Merritts, D.J., Snyder, N.P., Bierman, P., Sanquini, A., Fosdick, J.C., and Hilley, G.E., 2018, Erosion of coastal drainages in the Mendocino Triple Junction region (MTJ), northern California: Earth and Planetary Science Letters, v. 502, p. 156–165, https://doi.org/10.1016/j.epsl.2018.09.006.

Morton, D.M., Alvarez, R.M., Ruppert, K.R., and Goforth, B., 2008, Contrasting rainfall generated debris flows from adjacent watersheds at Forest Falls, southern California, USA: Geomorphology, v. 96, p. 322–338, https://doi.org/10.1016/j.geomorph.2007.03.021.

Nicholson, C., Sorlien, C.C., Atwater, T., Crowell, J.C., and Luyendyk, B.P., 1994, Microplate capture, rotation of the western Transverse Ranges, and initiation of the San Andreas transform as a low-angle fault system: Geology, v. 22, p. 491–495, https://doi.org/10.1130/0091-7613(1994)022<0491:MCROTW>2.3.CO;2.

Niemi, T.M., and Hall, N.T., 1992, Late Holocene slip rate and recurrence of great earthquakes on the San Andreas Fault in northern California: Geology, v. 20, p. 195–198, https://doi.org/10.1130/0091-7613(1992)020<0195:LHSRAR>2.3.CO;2.

Nishiizumi, K., Imamura, M., Caffee, M.W., Southon, J.R., Finkel, R.C., and McAninch, J., 2007, Absolute calibration of ^{10}Be AMS standards: Nuclear Instruments & Methods in Physics Research Section B: Beam Interactions with Materials and Atoms, v. 258, p. 403–413, https://doi.org/10.1016/j.nimb.2007.01.297.

Norton, K.P., von Blanckenburg, F., Schlunegger, F., Schwab, M., and Kubik, P.W., 2008, Cosmogenic nuclide-based investigation of spatial erosion and hillslope channel coupling in the transient foreland of the Swiss Alps: Geomorphology, v. 95, p. 474–486, https://doi.org/10.1016/j.geomorph.2007.07.013.

Oberlander, T.M., 1972, Morphogenesis of granitic boulder slopes in the Mojave Desert, California: The Journal of Geology, v. 80, p. 1–20, https://doi.org/10.1086/627710.

Owen, L.A., Finkel, R.C., Minnich, R.A., and Perez, A.E., 2003, Extreme southwestern margin of late Quaternary glaciation in North America: Timing and controls: Geology, v. 31, p. 729–732, https://doi.org/10.1130/G19561.1.

Owen, L.A., Clemmens, S.J., Finkel, R.C., and Gray, H., 2014, Late Quaternary alluvial fans at the eastern end of the San Bernardino Mountains, Southern California: Quaternary Science Reviews, v. 87, p. 114–134, https://doi.org/10.1016/j.quascirev.2014.01.003.

Perron, J.T., and Royden, L., 2013, An integral approach to bedrock river profile analysis: Earth Surface Processes and Landforms, v. 38, p. 570–576, https://doi.org/10.1002/esp.3302.

Portenga, E.W., Bierman, P.R., Duncan, C., Corbett, L.B., Kehrwald, N.M., and Rood, D.H., 2015, Erosion rates of the Bhutanese Himalaya determined using in situ-produced ^{10}Be: Geomorphology, v. 233, p. 112–126, https://doi.org/10.1016/j.geomorph.2014.09.027.

Sadler, P.M., and Reeder, W.A., 1983, Upper Cenozoic, quartzite-bearing gravels of the San Bernardino Mountains, southern California: Recycling and mixing as a result of transpressional uplift, *in* Anderson, D.W., and Rymer, M.J., eds., Tectonics and Sedimentation along the Faults of the San Andreas System: Pacific Section, Society for Sedimentary Geology (SEPM), p. 45–57.

Scherler, D., and Schwanghart, W., 2020a, Drainage divide networks—Part 1: Identification and ordering in digital elevation models: Earth Surface Dynamics, v. 8, p. 245–259, https://doi.org/10.5194/esurf-8-245-2020.

Scherler, D., and Schwanghart, W., 2020b, Drainage divide networks—Part 2: Response to perturbations: Earth Surface Dynamics, v. 8, p. 261–274, https://doi.org/10.5194/esurf-8-261-2020.

Schwanghart, W., and Scherler, D., 2014, TopoToolbox 2–MATLAB-based software for topographic analysis and modeling in Earth surface sciences: Earth Surface Dynamics, v. 2, p. 1–7, https://doi.org/10.5194/esurf-2-1-2014.

Simoes, M., Sassolas-Serrayet, T., Cattin, R., Roux-Mallouf, L., Ferry, M., and Drukpa, D., 2021, Topographic disequilibrium, landscape dynamics and active tectonics: An example from the Bhutan Himalaya: Earth Surface Dynamics, v. 9, p. 895–921, https://doi.org/10.5194/esurf-9-895-2021.

Spotila, J.A., Farley, K.A., and Sieh, K., 1998, Uplift and erosion of the San Bernardino Mountains associated with transpression along the San Andreas Fault, California, as constrained by radiogenic helium thermochronometry: Tectonics, v. 17, p. 360–378, https://doi.org/10.1029/98TC00378.

Spotila, J.A., Farley, K.A., Yule, J.D., and Reiners, P.W., 2001, Near-field transpressive deformation along the San Andreas Fault zone in southern California, based on exhumation constrained by (U-Th)/He dating: Journal of Geophysical Research: Solid Earth, v. 106, p. 30,909–30,922, https://doi.org/10.1029/2001JB000348.

Spotila, J.A., House, M.A., Blythe, A.E., Niemi, N.A., Bank, G.C., and Barth, A., 2002, Controls on the erosion and geomorphic evolution of the San Bernardino and San Gabriel Mountains, southern California, *in* Barth, A., ed., Contributions to Crustal Evolution of the Southwestern United States: Geological Society of America Special Paper 365, p. 205–230, https://doi.org/10.1130/0-8137-2365-5.205.

Stone, J.O., 2000, Air pressure and cosmogenic isotope production: Journal of Geophysical Research: Solid Earth, v. 105, p. 23,753–23,759, https://doi.org/10.1029/2000JB900181.

Weldon, R.J., 2010, Slip rate for the North Branch of the San Andreas Fault, San Bernardino Valley: Southern California Earthquake Center, v. 1.

Weldon, R.J., and Sieh, K.E., 1985, Holocene rate of slip and tentative recurrence interval for large earthquakes on the San Andreas Fault, Cajon Pass, southern California: Geological Society of America Bulletin, v. 96, p. 793–812, https://doi.org/10.1130/0016-7606(1985)96<793:HROSAT>2.0.CO;2.

Whipple, K.X., and Tucker, G.E., 1999, Dynamics of the stream-power river incision model: Implications for height limits of mountain ranges, landscape response timescales, and research needs: Journal of Geophysical Research: Solid Earth, v. 104, p. 17,661–17,674, https://doi.org/10.1029/1999JB900120.

Whipple, K.X., Forte, A.M., DiBiase, R.A., Gasparini, N.M., and Ouimet, W.B., 2017, Timescales of landscape response to divide migration and drainage capture: Implications for the role of divide mobility in landscape evolution: Journal of Geophysical Research: Earth Surface, v. 122, p. 248–273, https://doi.org/10.1002/2016JF003973.

Willenbring, J.K., Gasparini, N.M., Crosby, B.T., and Brocard, G., 2013, What does a mean mean?: The temporal evolution of detrital cosmogenic denudation rates in a transient landscape: Geology, v. 41, p. 1215–1218, https://doi.org/10.1130/G34746.1.

Willett, S.D., McCoy, S.W., Perron, J.T., Goren, L., and Chen, C.-Y., 2014, Dynamic reorganization of river basins: Science, v. 343, https://doi.org/10.1126/science.1248765.

Wright, T.L., 1991, Structural geology and tectonic evolution of the Los Angeles Basin, California, *in* Biddle, K.T., ed., Active Margin Basins: American Association of Petroleum Geologists Memoir 52, p. 35–134, https://doi.org/10.1306/M52531C3.

Yang, R., Willett, S.D., and Goren, L., 2015, In situ low-relief landscape formation as a result of river network disruption: Nature, v. 520, p. 526–529, https://doi.org/10.1038/nature14354.

Science Editor: Mihai Ducea
Associate Editor: Emmanuel Gabet

Manuscript Received 24 August 2022
Revised Manuscript Received 17 March 2023
Manuscript Accepted 23 June 2023

Printed in the USA